

The Value of Assimilating Different Ground-Based Profiling Networks on the Forecasts of Bore-Generating Nocturnal Convection

HRISTO G. CHIPILSKI, ^{a,b} XUGUANG WANG, ^a DAVID B. PARSONS, ^a AARON JOHNSON, ^a AND SAMUEL K. DEGELIA ^a

^a School of Meteorology, University of Oklahoma, Norman, Oklahoma ^b Advanced Study Program, National Center for Atmospheric Research, Boulder, Colorado

(Manuscript received 21 July 2021, in final form 12 January 2022)

ABSTRACT: There is a growing interest in the use of ground-based remote sensors for numerical weather prediction, which is sparked by their potential to address the currently existing observation gap within the planetary boundary layer. Nevertheless, open questions still exist regarding the relative importance of and synergy among various instruments. To shed light on these important questions, the present study examines the forecast benefits associated with several different ground-based profiling networks using 10 diverse cases from the Plains Elevated Convection at Night (PECAN) field campaign. Aggregated verification statistics reveal that a combination of in situ and remote sensing profilers leads to the largest increase in forecast skill, in terms of both the parent mesoscale convective system and the explicitly resolved bore. These statistics also indicate that it is often advantageous to collocate thermodynamic and kinematic remote sensors. By contrast, the impacts of networks consisting of single profilers appear to be flow-dependent, with thermodynamic (kinematic) remote sensors being most useful in cases with relatively low (high) convective predictability. Deficiencies in the data assimilation method as well as inherent complexities in the governing moisture dynamics are two factors that can further limit the forecast value extracted from such networks.

KEYWORDS: Data assimilation; Remote sensing; Convective-scale processes

1. Introduction

The planetary boundary layer (PBL) has crucial implications for many Earth system processes, such as radiative transfer, air pollution, and land-atmosphere exchanges (Wulfmeyer et al. 2015). Compared to other parts of the atmosphere, the PBL is characterized by considerably smaller spatiotemporal scales, especially with respect to water-related variables (Lilly and Perkey 1976). To adequately describe the inherently large variability in the PBL, one requires a dense observing network that can frequently sample the thermodynamic and kinematic properties of the lower atmosphere. Nevertheless, the PBL is observed poorly by current observing systems—a fact that became first apparent in early studies of convection initiation. For example, Crook (1996) used a high-resolution, nonhydrostatic model to show that small changes in the PBL structure, comparable in magnitude to typical measurement uncertainties, "can make the difference between no initiation and intense convection." Similarly, Weckwerth et al. (1996) found that there is large moisture variability within daytime PBLs $(1.5-2.5 \text{ g kg}^{-1})$, concluding that water vapor is under-sampled by traditional observation techniques (see also Weckwerth and Parsons 2006). Having realized these limitations, the National Research Council (NRC) developed a comprehensive report in 2009, which proposed the establishment of 400 sites with

 ${\it Corresponding\ author}. \ Dr.\ Hristo\ G.\ Chipilski, hristoc@ucar.edu$

ground-based remote sensors (NRC 2009). These recommendations were further refined in subsequent NRC reports (NRC 2010, 2012) and recently updated by the World Meteorological Organization (WMO 2018) to address the needs of future high-resolution numerical weather prediction (NWP) systems.

Importantly, the growing awareness of the PBL's observation gap catalyzed research efforts aimed at examining the ability of various ground-based remote sensors to improve regional NWP performance. At the beginning, the technology underpinning thermodynamic remote sensors was still not sufficiently developed and most of the original investigations were conducted with the more widely available radar wind profiler (RWP). After several studies demonstrated the shortrange forecast value coming from the National Oceanic and Atmospheric Administration (NOAA) Profiler Network (NPN), some of the leading NWP centers began assimilating these novel wind datasets (Bouttier 2001; Benjamin et al. 2004). Recently, experiments have also been conducted with another kinematic profiler—the Doppler wind lidar (DWL), whose ability to capture the fine-scale structure of the wind field makes it particularly suitable for use in high-resolution numerical models. The forecast potential of DWL retrievals was first demonstrated by Zhang and Pu (2011) on a warmseason mesoscale convective system (MCS). Kawabata et al. (2014) confirmed the NWP value of this instrument and

further discussed the important synergy between lidar and radar observations in improving the overall convective skill.

The microwave radiometer (MWR) was the first thermodynamic remote sensor to be used in NWP applications, including fog forecasting (Vandenberghe and Ware 2002), 1D-Var retrievals (Martinet et al. 2015, 2017), and heavy precipitation (Caumont et al. 2016). Although its ability to operate under allsky conditions is an important advantage, the MWR resolution (300–1000 m in the first 2 km AGL) is too coarse relative to the vertical grid spacing of most convection-allowing models. As a result, recent impact studies have focused on exploring the advantages of another passive thermodynamic remote sensor-the Atmospheric Emitted Radiance Interferometer (AERI), and have demonstrated that its assimilation can be beneficial for a variety of convective applications (Coniglio et al. 2019; Hu et al. 2019; Chipilski et al. 2020; Degelia et al. 2020; Lewis et al. 2020). Concurrently, the past decade has also seen advances in active thermodynamic sensing. Instruments like the Raman lidar (RL) and the differential absorption lidar (DIAL) have been crucial in improving our understanding of near-surface Earth system processes (Wulfmeyer et al. 2015, and references therein). Researchgrade RLs have been found to improve the simulated PBL structure (Adam et al. 2016; Grzeschik et al. 2008) and the ability of regional NWP models to predict heavy precipitation (Leuenberger et al. 2020; Yoshida et al. 2020).

In this paper, we provide more evidence for the NWP value of ground-based remote sensors by demonstrating their systematic benefits on the relatively newly studied problem of bore-generating nocturnal convection (Haghi et al. 2018; Parsons et al. 2019). This goal is achieved by using 10 diverse cases from the Plains Elevated Convection at Night (PECAN; Geerts et al. 2017) field campaign. Many of the simulated events have been examined in great detail as part of recent publications (e.g., Mueller et al. 2017; Trier et al. 2017; Johnson et al. 2018; Johnson and Wang 2019; Smith et al. 2019; Miller et al. 2020; Parker et al. 2020; Stechman et al. 2020; Carroll et al. 2021; Lin et al. 2021), which provides an important context for our results. In addition, the forecast impacts presented here corroborate the single case findings of Chipilski et al. (2020; CWP20 hereafter); this is a highly encouraging finding given the wide spectrum of atmospheric bores and convective environments sampled in our dataset.

By further refining the experimental design of CWP20, the second important contribution of this study is examining the relative benefits of different ground-based profiling networks. The motivation here is that most research in the past has focused on the assimilation of single remote sensors that can only measure the thermodynamic or kinematic components of the unknown model state (e.g., Lewis et al. 2020; Li et al. 2020; Yoshida et al. 2020; Wang et al. 2020; Leuenberger et al. 2020; Qi et al. 2021). While several studies have attempted to simultaneously assimilate multiple profiling instruments, they have reached somewhat inconsistent conclusions. For instance, Hu et al. (2019) found AERIs to be more important than DWLs in improving the early evolution of a tornadic supercell. At the same time, the study of Fourriè et al. (2021) indicated that forecasts of heavy precipitation were improved more by assimilating RWPs compared to RLs. A careful look

at the present literature reveals that even fewer studies have attempted to evaluate the impacts of remote sensors against a reference radiosonde network. Throughout this work, we will demonstrate that the benefits of assimilating thermodynamic and kinematic remote sensors tend to be flow-dependent and that their combination is often necessary for achieving a statistically meaningful increase in the forecast skill. We will also present evidence that the most robust forecast benefits come from hybrid ground-based networks that contain both in situ and remote sensing profilers.

2. Problem statement

In this study, we will be concerned with the forecast accuracy of a particular class of nocturnal convection—one associated with the generation of atmospheric bores (bore-generating nocturnal convection hereafter). Our interest in these convective systems was motivated by their common occurrence during the night (Haghi et al. 2017) and inherently low predictability (see section 1 of CWP20). Figure 1 illustrates the typical evolution of bore-generating nocturnal convection within the 10 PECAN cases used herein. The data assimilation (DA) period usually covered the time from the initial formation of convective cells (Fig. 1a) to their upscale growth and eventual merging into a mesoscale convective system (MCS) with a well-developed surface-based cold pool (Fig. 1b). It is worth noting that while surface-based cold pools do not necessarily form in all nocturnal MCSs (e.g., Maddox 1980; Trier and Parsons 1993), they occurred commonly during PECAN (Hitchcock et al. 2019) and were an important precursor for the initiation of bores in our experiments.

A critical requirement for our case study selection was the presence of ground-based profilers upstream of the convective developments displayed in Figs. 1a and 1b. Because of their strategic deployment, these PECAN instruments provided valuable information about the mesoscale environment in which the bore-generating convective systems developed. Therefore, it was expected that their assimilation would also bring measurable forecast improvements. Our dynamically relevant DA period was chosen to help us evaluate this hypothesis in a controlled manner: by creating initial conditions that featured a mature MCS with a well-developed cold pool, we ensured that the future evolution of the convective system will be mostly driven by the characteristics of the environment into which it propagates. By contrast, if the forecasts were to be initialized earlier, the MCS evolution will be sensitive to the highly nonlinear (and inherently unpredictable) small-scale interactions between individual convective cells (see Fig. 1a), making it challenging to quantify the value of different ground-based profiling networks.

Once the DA period was complete, we forecasted the boregenerating MCS for another 5 h. During this time, the interaction between its cold pool and the nocturnal PBL generated a hydraulic response in the form of an atmospheric bore (Fig. 1c). In some of the simulated cases, the bore remained closely attached to its parent MCS and was responsible for the initiation of new convection (i.e., bore-initiated convection), whereas in other cases, it propagated far away from its source region and

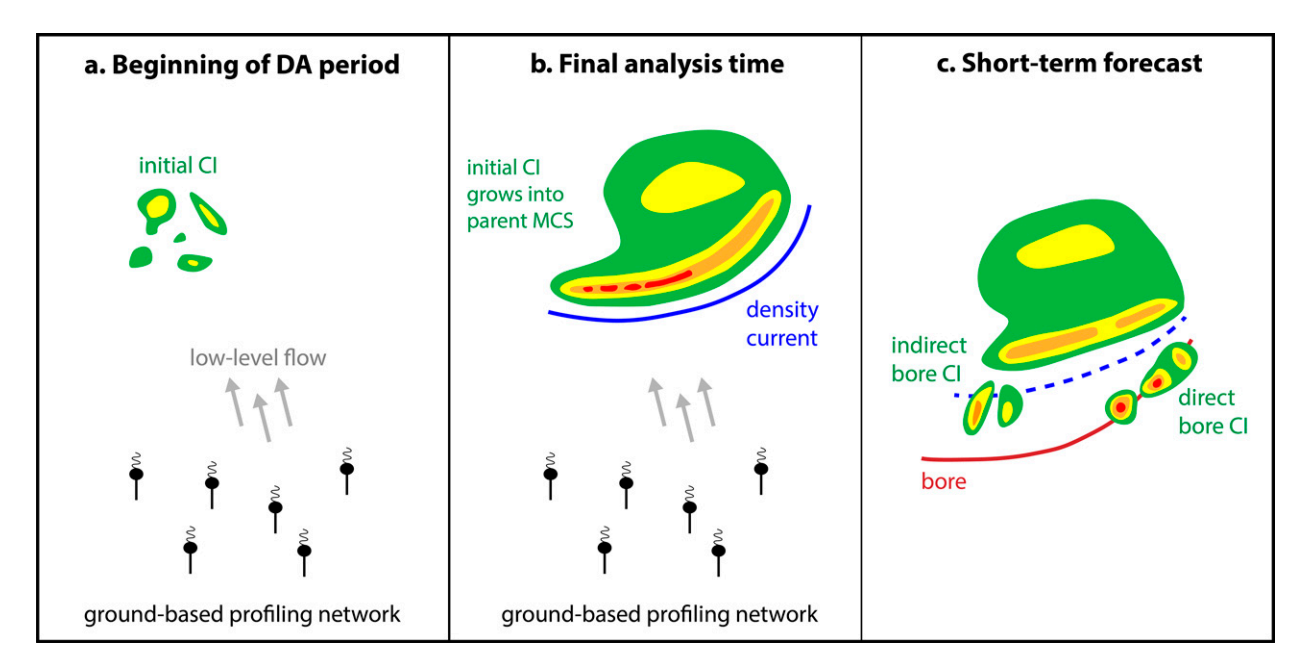


FIG. 1. A schematic illustrating the typical evolution of a bore-generating convective system in the context of the ground-based profiling instruments assimilated in this study. Our main objective is to evaluate the impact of the assimilated profilers on the forecasted parent MCS, bore-induced convection initiation (CI; both direct and indirect) and explicitly resolved atmospheric bore [all shown in (c)].

did not produce additional convective activity. To account for this inherent dynamical coupling between the bore and its parent MCS, we adopted a verification approach similar to CWP20 whereby the impact from different profiling instruments was examined according to their ability to improve both the convective and bore components of the nocturnal system depicted in Fig. 1c.¹

3. Experimental design

To better understand the synergies between different ground-based profiling networks, we refined the experimental design of CWP20 such that only sites with collocated radiosondes and remote sensors were assimilated. This approach resembles the methodology of Degelia et al. (2020) except that our control experiments did not assimilate any PECAN soundings. The rationale behind this choice was that the PECAN radiosondes are released at a much higher frequency compared to the operational radiosonde network, meaning that they can no longer be treated as a conventional data source. Degelia et al. (2020) sidestepped this problem by only assimilating observations close to the operational 0000 UTC launch; in our case, all available radiosondes were assimilated and subsequently treated as a reference against which the performance of ground-based remote sensors can be evaluated.

Our ground-based network with collocated in situ and remote sensing instruments serves two distinct purposes. First, it allows us to compare the impacts from remote sensors and radiosondes in a more objective way that eliminates the increased (or decreased) sensitivity of the forecasts to the initial conditions in different parts of the model domain. Given that the PECAN instruments observe the environmental conditions over the same location, differences in their performance can be solely attributed to the underlying measurement technique, sampling rate and observation error characteristics. The second advantage of assimilating collocated instruments is that we can explore the benefits of several different ground-based profiling networks and seek answers to the following relevant questions:

- Is it more beneficial to assimilate the highly frequent, but less accurate remote sensing retrievals than the less frequent, but highly accurate radiosonde measurements?
- How competitive is the performance of networks that consist of single remote sensors compared to networks that host both thermodynamic and kinematic profilers?
- Do we observe synergies after combining (i) thermodynamic and kinematic profilers or (ii) remote sensing and in situ instruments? In other words, does the simultaneous assimilation of these instruments result in forecast improvements which are much larger than the forecast improvements brought by individual instruments?

a. PECAN observations

The profilers assimilated in our study were obtained from five fixed and two mobile PECAN Integrated Sounding Arrays (PISAs; see Figs. 2a,b). These PISAs were a unique aspect of the PECAN field campaign as they hosted both in situ and remote sensing instruments. Analogous to CWP20, AERI was the only thermodynamic profiler assimilated in

¹ The main difference with CWP20 was that our verification included both the parent MCS and any bore-initiated convection, whereas CWP20 only focused on the latter.

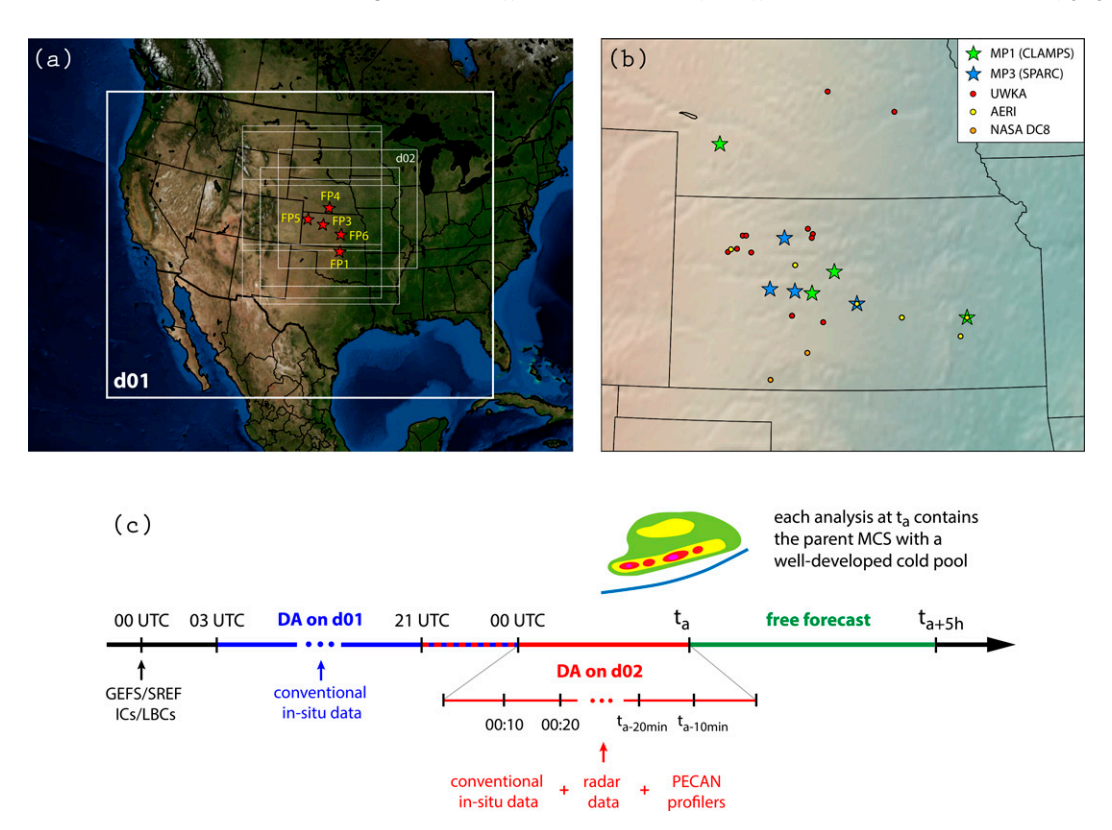


FIG. 2. Some aspects of the experimental design used in this study. (a) Location of the outer 12-km (d01; thick white rectangle) and inner 4-km (d02; thinner white rectangles) model domains as well as the assimilated fixed PISA (FP) sites (red stars). (b) Location of the assimilated mobile PISAs (MPs) (filled stars) and thermodynamic remote sensors used for bore verification (filled dots). (c) A timeline corresponding to our analysis–forecast system. Following section 2, the final analysis time in each PECAN case (t_a) is chosen such that the bore-generating (parent) MCS has a well-developed cold pool. The alternating red and blue lines between 2100 and 0000 UTC indicate that the d02 EnKF cycling can begin at either of these two times (see main text for more details).

this paper, whereas the RWPs and DWLs were blended into a single kinematic profiler following Degelia et al. (2020).

The number of PISA sites available for each case was based on the overall availability of PECAN radiosonde data. Specifically, a certain PISA site was assimilated in our experiments only if there was at least one radiosonde release from that site during the selected DA period. As a result of this restriction, the number of assimilated stations was usually reduced to 3 or 4 (see Table 2). At each of the assimilated PISA sites, the typical number of radiosonde launches was between 3 and 5, although on one occasion (20 June), the FP3 site released a total of 13 radiosondes over the 7-h DA period.

b. System configurations

The impact results presented here were obtained with the same GSI-EnKF-WRF ensemble data assimilation and forecast system as described in CWP20 (see also Johnson et al. 2015; Wang and Wang 2017). However, the systematic nature of our PECAN experiments necessitated several minor changes in its configuration. Most notably, simulations were carried out on two (instead of three) model domains (Fig. 2a)—an outer (d01) 12-km one and an inner (d02) 4-km one. The size of the d02 domains was the same for all 10 cases (352 × 301 grid points),

but their position was modified according to the location of the bore-generating convective systems. The model physics were chosen to be broadly consistent with CWP20 except from several changes which can be identified by comparing Table 1 here and Table 2 in CWP20.

All experiments were initialized by downscaling the 0000 UTC global GEFS/SREF ensemble (40 members in total) valid on the day before each bore-generating MCS event (see Fig. 2c). Conventional observations from the North American Mesoscale Forecast System Data Assimilation System (NDAS) were then assimilated every 3 h for a total of 8 cycles. Afterward, much more frequent EnKF cycling was carried out on the inner 4-km domain where conventional observations were assimilated together with radar data and PECAN ground-based profilers at 10-min intervals. As explained in section 2, the length of the inner DA window was dependent on the convective evolution in each case, but varied between 2.5 h on 16 July 2015 and 7 h on 20 June 2015 (see Table 2 for more details). For the majority of the PECAN cases, the d02 EnKF cycling started at 0000 UTC on the day of the bore-generating MCS event; one exception to this setup was the 7 June case where the 4-km DA period began 3 h earlier to account for the early convection initiation on that day.

TABLE 1. List of WRF (version 3.8) physics options.

Parameterization	Scheme	Reference
Microphysics (EnKF cycling)	WRF single-moment 6-class (WSM6)	Hong and Lim (2006)
Microphysics (forecast)	Thompson	Thompson et al. (2008)
Planetary boundary layer and surface layer	Mellor–Yamada–Nakanishi–Niino (MYNN)	Nakanishi and Niino (2006)
Land surface	Unified Noah land surface model	Tewari et al. (2004)
Longwave radiation	Rapid Radiative Transfer Model for GCMs (RRTMG)	Iacono et al. (2008)
Shortwave radiation	Goddard shortwave;	Chou and Suarez (1994)
Cumulus (d01 domain only)	Kain-Fritsch, Grell-Freitas ensemble and, Grell 3D ensemble	Kain (2004); Grell and Freitas (2014); Grell and Devenyi (2002)

c. Experiments

To examine the value of different ground-based profiling networks, we adopted a data addition framework whereby each new PECAN instrument was added on top of operationally assimilated NDAS data. The first group of experiments only considered single instrument types: SONDE assimilated the special PECAN radiosondes, TQPROF—the thermodynamic AERI retrievals, and UVPROF-the wind retrievals from the combined DWL and RWP instruments. By contrast, the second group of experiments sought to explore the value of multiple profilers and to identify the existence of observation synergies. For instance, ALLPROF combined the two types of ground-based remote sensors, whereas ALL considered all available PECAN observations for a given case. The performance of these five ground-based profiling networks was then compared against a control (CTL) experiment in which only conventional NDAS data were assimilated.

4. Results

a. Convective impacts

1) AGGREGATED STATISTICS

We first assessed the profiler impacts with respect to the convective forecasts. For each of the 10 cases, we computed the Fractions Skill Score (FSS) based on the Neighborhood

Ensemble Probability (NEP) of radar reflectivity exceeding 30 dBZ and the merged composite reflectivity product from the Multi-Radar Multi-Sensor (MRMS; Zhang et al. 2016) program. These scores were evaluated at 15-min increments within verification subdomains centered over the bore-generating MCSs. The position and size of these subdomains varied from case to case, but they were subjectively drawn to encompass both the parent MCS and any bore-initiated convection during the entire 5-h simulation period.

Figure 3 displays the aggregated FSSs for 3 different neighborhood radii (R)—5, 25, and 150 km. Each of these scores carries a different physical meaning. For example, the smallest R value is comparable to the model's horizontal grid spacing, in which case the FSSs provide a point-wise measure of the convective skill. The intermediate R value is commensurate with the smallest scales resolved by the model ($\sim 8\Delta x$), whereas the largest one is located toward the upper end of the meso- β spectrum, making it comparable to the scale of large density currents and bores (Zuidema et al. 2017). As expected, the FSSs increased with R for a given forecast lead time, correctly reflecting the higher predictability of the larger scales. On average, the experimental differences persisted for ~ 2 h, although this period tended to be slightly longer as R increased.

Regardless of the chosen verification scale, ALL provided the best forecast performance, with the FSS differences being

TABLE 2. EnKF cycling period and assimilated PISA sites for the 10 PECAN cases used in this study. The numbers in the last seven columns of the table indicate how many radiosondes were launched at each of the assimilated PISA sites.

EnKF cycling on the d02 domain			Assimilated PISA sites						
Case	Start	End	FP1	FP3	FP4	FP5	FP6	MP1	MP3
5 Jun 2015	0000 UTC 5 Jun	0430 UTC 5 Jun	×	1	1	×	×	×	×
6 Jun 2015	0000 UTC 6 Jun	0330 UTC 6 Jun	×	1	1	×	×	×	1
7 Jun 2015	2100 UTC 6 Jun	0200 UTC 7 Jun	1	×	×	×	×	X	×
20 Jun 2015	0000 UTC 20 Jun	0700 UTC 20 Jun	×	13	4	×	×	4	5
26 Jun 2015	0000 UTC 26 Jun	0300 UTC 26 Jun	×	2	×	2	×	1	×
2 Jul 2015	0000 UTC 2 Jul	0300 UTC 2 Jul	×	1	1	1	×	×	×
5 Jul 2015	0000 UTC 5 Jul	0500 UTC 5 Jul	×	2	2	×	2	2	×
11 Jul 2015	0000 UTC 11 Jul	0600 UTC 11 Jul	×	4	4	4	5	3	3
14 Jul 2015	0000 UTC 14 Jul	0300 UTC 14 Jul	×	2	2	2	2	×	×
16 Jul 2015	0000 UTC 16 Jul	0230 UTC 16 Jul	×	3	3	2	3	×	2

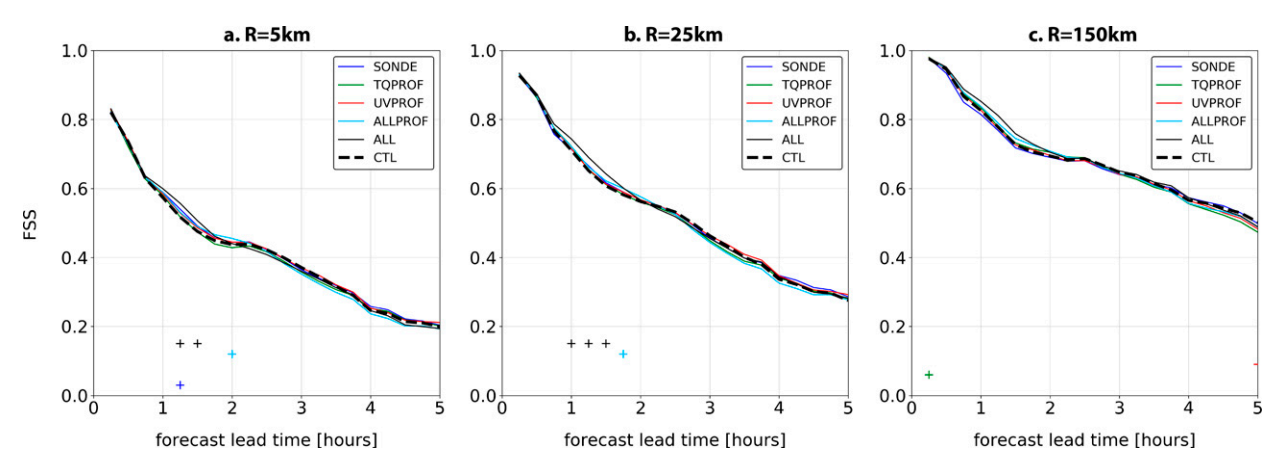


FIG. 3. Fractions skill scores (FSSs) averaged over the 10 PECAN cases and calculated for three different neighborhood radii: (a) 5, (b) 25, and (c) 150 km. The markers at the bottom of each panel indicate whether the FSS differences between a given PECAN experiment and CTL are statistically significant at the α = 0.01 level, as determined by a bootstrap method with 10,000 resamples. The + and – symbols differentiate between positive and negative impacts, respectively.

statistically significant at smaller *R* and for forecast lead times between 1 and 2 h. Given that the forecast skill at these smaller scales was completely lost toward the end of the 5-h forecasting window,² our verification statistics indicate that the analysis benefits brought by ALL lasted for more than 30% of the typical convective predictability time scale in CTL. Another interesting aspect of these aggregated statistics is the similarity of the FSSs at the start of the forecasting period—a result which is opposite to some of the findings reported in Degelia et al. (2020, e.g., see their Fig. 4). The comparable short-term performance of CTL and ALL in our study implies that the environmental perturbations brought by the assimilation of PECAN profilers required additional growth before being able to impact the subsequent convective evolution.

Some marginal improvements were also observed with respect to ALLPROF, although those were considerably smaller and shorter-lived. While the most pronounced ALLPROF benefits occurred at R=150 km (where ALLPROF was nearly as skillful as the best-performing ALL experiment), the FSS differences at this verification radius were not statistically significant.

The impacts from single profiler experiments (SONDE, TQPROF and UVPROF) were generally smaller than ALL and ALLPROF. In addition, the verification statistics of these experiments were more sensitive to the chosen verification radius: they improved upon the CTL skill at R=5 km (especially SONDE), but their impacts at larger R values became neutral or even slightly negative.

To test the extent to which the presented impacts depend on the chosen verification subdomains, aggregate FSS statistics were also computed over the entire d02 domain. While the experimental differences were considerably smaller in this case, the positive impacts from ALL were still present during the first 2 h of the forecast. This is a very promising result as it implies that the assimilation of ground-based profilers had domain-wide benefits on the convective forecasts.

2) FLOW DEPENDENCE OF THE FORECAST IMPACTS

One of the most interesting aspects of this systematic study was the strong variability of the convective skill. To understand how this variability modulated the impacts discussed so far, the 10 PECAN cases were split into 3 predictability categories based on the 2-h FSS associated with the CTL experiment (see Fig. 4). The choice of this specific lead time was motivated by the fact that the least predictable PECAN cases tended to completely lose their convective skill 2 h into the forecast (Fig. 4a). On the other hand, this predictability definition is also consistent with the duration of the largest experimental differences in the aggregated FSS statistics, as evident in Fig. 3. One notable exception to this rule was the HP cases where the experimental differences started to grow only after 2 h of model integration (Fig. 4c).

Differences in the forecast impacts for each predictability category are visualized through the violin plots in Fig. 5. The color shaded distributions in each panel show the FSS differences between a certain PECAN experiment and CTL. Similar to the average FSS results, ALL continues to be the best performing experiment in the low predictability (LP) category (5, 11, and 14 July), with the largest contributions coming from TQPROF. We also observe that ALLPROF performed slightly worse than TQPROF, indicating that the addition of kinematic profilers degraded the forecasts. This is to be contrasted with the high predictability (HP) category (6 June, 7 June, 20 June, and 2 July) where UVPROF achieved the highest FSSs, while the addition of other profiling instruments in ALLPROF and ALL decreased the overall convective skill. On average, both TQPROF and UVPROF had a slightly negative impact in the medium predictability (MP) category (5 June, 26 June, and 16 July), whereas their combined assimilation produced a visible improvement in the convective skill. Together with the positive impacts in SONDE, this finding indicates the importance of

² The loss of convective skill is evident in the small FSS changes at the end of the forecasting window. Error saturation for R = 5 km, for instance, occurs when the lead time is 4.5 h.

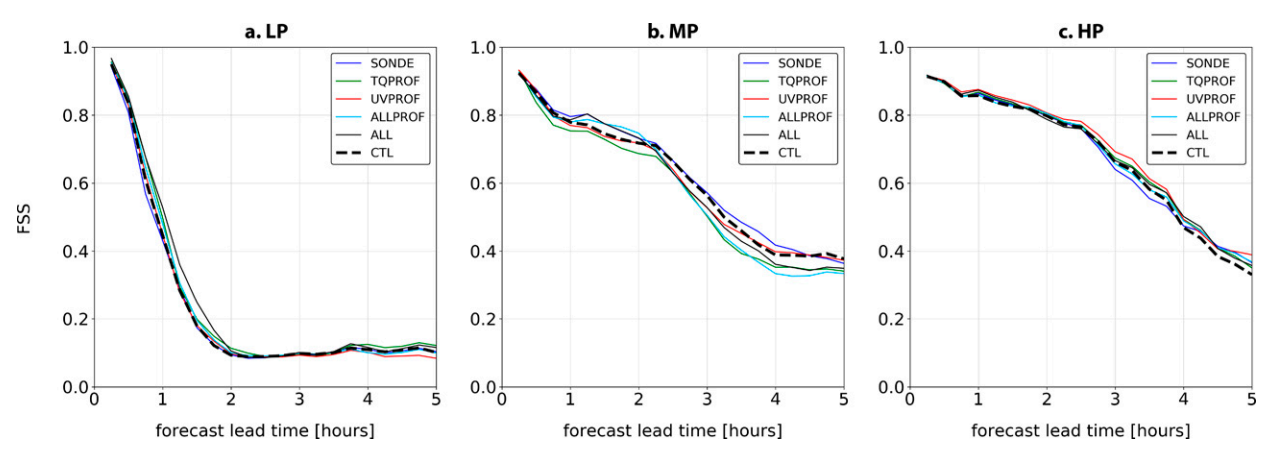


FIG. 4. As in Fig. 3, but the FSSs here are conditioned on the three predictability categories—(a) LP, (b) MP, and (c) HP (see main text for more details)—and are only shown for R = 25 km. Note that statistical significance has not been tested here due to the small number of cases in each predictability category.

simultaneously observing the thermodynamic and kinematic components of the model state in the MP cases.

b. Bore impacts

1) VERIFICATION METHODOLOGY

Atmospheric bores are particularly challenging to identify and track due to their complex footprint on several meteorological variables. Even though some NWP-based algorithms have been proposed in the past (e.g., Chipilski et al. 2018), the objective detection of bores in observational datasets remains elusive. Albeit these limitations, our study attempts to provide a comprehensive assessment of how the assimilation of different ground-based profiling networks affects the forecast skill of explicitly resolved bores. Toward this end, ensemble mean forecasts from the simulated PECAN cases were verified in two different ways. Similar to Geerts et al. (2017, see their Fig. 8), we first examined the spatial representation of bores by comparing model fields of vertical velocity at 1 km AGL (w_{1km}) against the position of fine lines in low-level radar reflectivity data. This methodology resembles the one utilized by Wilson and Roberts (2006) and aims to examine the realism

of various simulated bore attributes, including position, extent and propagation direction.

Our second verification method examined the extent to which the ensemble mean forecasts were able to accurately simulate the amount of bore lifting (Δh) , i.e., the difference between the post and pre-bore PBL heights. The choice of this metric was motivated by its relevance to the initiation and maintenance of nocturnal convection: a larger Δh value translates to more pronounced mechanical lifting at the leading edge of the bore, which in turn creates more favorable conditions for air parcels to reach their level of free convection. To estimate Δh , we followed Chipilski et al. (2018) and searched for the water vapor mixing ratio (q) or virtual potential temperature (θ_v) contour associated with the largest vertical displacement near the ground. Aside from the University of Wisconsin King Air (UWKA) moisture retrievals used in CWP20, our bore verification dataset featured additional thermodynamic profiles from ground-based AERI sites as well as moisture retrievals from the National Aeronautics and Space Administration (NASA) DC-8 aircraft. All 20 Δh measurements (see filled circles in Fig. 2b) were then compared to model-derived Δh estimates from vertical cross sections generated in proximity to the observed bore locations.

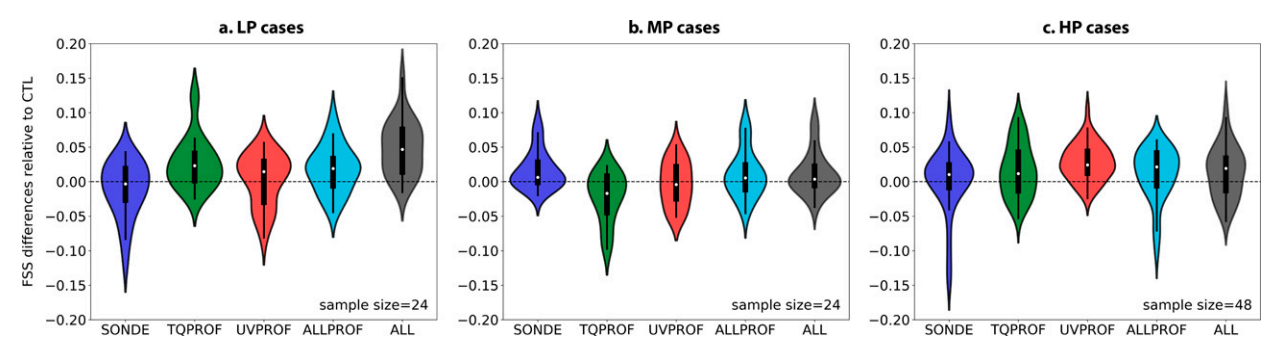


Fig. 5. Violin plots showing the predictability-dependent FSS differences between the five PECAN experiments and CTL. The (a) LP and (b) MP cases combine all FSS differences during the first 2 h, whereas the (c) HP category only considers lead times between 2 and 5 h when the experimental differences are more pronounced.

TABLE 3. Subjective evaluation of the forecast impacts pertaining to the spatial characteristics of the explicitly resolved bores; the + and - symbols denote positive and negative impacts, respectively. Some of the entries in the last column contain the word *synergy*, which indicates that the positive impacts in ALLPROF and/or ALL exceed those caused by the assimilation of single profiling instruments.

Case	CTL problems	Impacts in ALLPROF and ALL	Contribution from individual instruments
5 Jun 2015	Orientation	+ in both	+ from TQPROF and UVPROF; synergy
6 Jun 2015	Orientation, higher speed	+ in ALLPROF and - in ALL	+ from TQPROF and UVPROF; synergy
7 Jun 2015	Smaller extent	in ALLPROF and + in ALL	+ from SONDE and - from TQPROF; synergy
20 Jun 2015	No	No	_
26 Jun 2015	No	No	_
2 Jul 2015	No	No	_
5 Jul 2015	Maintenance, smaller extent	+ (extent) in both	+ from TQPROF; synergy (only in ALL)
11 Jul 2015	Maintenance, smaller extent	+ (maintenance) in ALLPROF and	+ from all; synergy
		+ (maintenance, extent) in ALL	
14 Jul 2015	Maintenance	+ in both	+ from TQPROF
16 Jul 2015	No	No	_

2) SPATIAL IMPACTS

The summary statistics in Table 3 indicate that the spatial structure of the simulated bores in CTL was consistent with the verifying radar observations in 4 out of the 10 cases. For the remaining 6 cases, the most common forecast issues pertained to the maintenance and extent of the predicted bores. Interestingly, these problems occurred most frequently in the LP regime where the parent MCSs tended to dissipate too quickly. This close relationship between the forecast skills of the bore and its parent MCS has a dynamical explanation; namely, the premature dissipation of the parent MCS leads to a weaker and shorter-lived cold pool that is in turn not capable of sustaining upstream-propagating disturbances for a very long time (see section 7 of White and Helfrich 2012). In the majority of these situations, the assimilation of ground-based profilers resulted in distinct forecast improvements. One such example comes from the 5 July case (Fig. 6) where ALL was able to successfully recover the eastern segment of the bore (originally missing in the CTL forecast). In agreement with the convective LP findings reported earlier in this Section, the largest contribution to this positive impact came from the TQPROF network.

The second, less common problem in CTL involved the *spatial orientation/propagation direction*³ of the explicitly resolved bores. Here the assimilation of PECAN profilers was also found to be helpful. Examining the 5 June case in Fig. 7, for instance, we see that CTL incorrectly simulated a southeastern- rather than a southwestern-propagating bore (cf. Figs. 7a,b). Similar to the 5 July case, the simultaneous assimilation of thermodynamic and kinematic remote sensors was essential for producing better forecast results (Fig. 7d); however, unlike the 5 July case, the inclusion of PECAN radiosondes did not bring any additional forecast benefits (cf. Figs. 7c,d).

3) STRUCTURAL IMPACTS

In Fig. 8, the Δh ensemble mean forecasts from all six experiments were objectively compared against the available bore observations. However, before commenting on the performance of different ground-based networks, it is worth noting that the average Δh value in our observational dataset (810.5 m) is commensurate with other recently published composite bore studies (Parsons et al. 2019; Loveless et al. 2019). Furthermore, the wide range of observed Δh values suggests that the thermodynamic profilers used here were able to sample a large variety of atmospheric bores.

Based on the Pearson correlation coefficient (r) values, there appears to be a weak positive linear relationship between the observed and simulated bore lifting values, but we also observe a relatively large scatter and negative bias, especially with respect to the high-amplitude bores. From the single profiler experiments (Figs. 8d–f), TQPROF led to the strongest forecast changes. However, the impacts from this ground-based network were not necessarily all positive: while TQPROF reduced the root-mean-square error (RMSE) by ~ 60 m and achieved the highest r value across all experiments, it further exacerbated the negative bias in CTL by ~ 10 m. On the other hand, the two combined ground-based networks (Figs. 8b,c) were able to improve all of the aforementioned verification metrics. They exhibited very similar performance, implying that the assimilation of radiosonde data on top of ground-based remote sensors had a negligible impact overall.

5. Case studies

The results from section 2 indicated that the forecast performance of SONDE, TQPROF, and UVPROF tends to be flow-dependent. To further explore the potential dependence of our findings on this aspect, we performed a detailed analysis of three representative PECAN cases whose main purpose was to establish a relationship between the forecast impacts of single profiler networks and the governing convective dynamics.

a. Low predictability case: 11 July 2015

For the LP category, we selected the 11 July case since its FSS time series was most representative of the average

³ A bore can propagate in several different directions. Therefore, to avoid ambiguity in the intended meaning of bore propagation, we use the propagation vector in the center of the observed and forecasted bore segments.

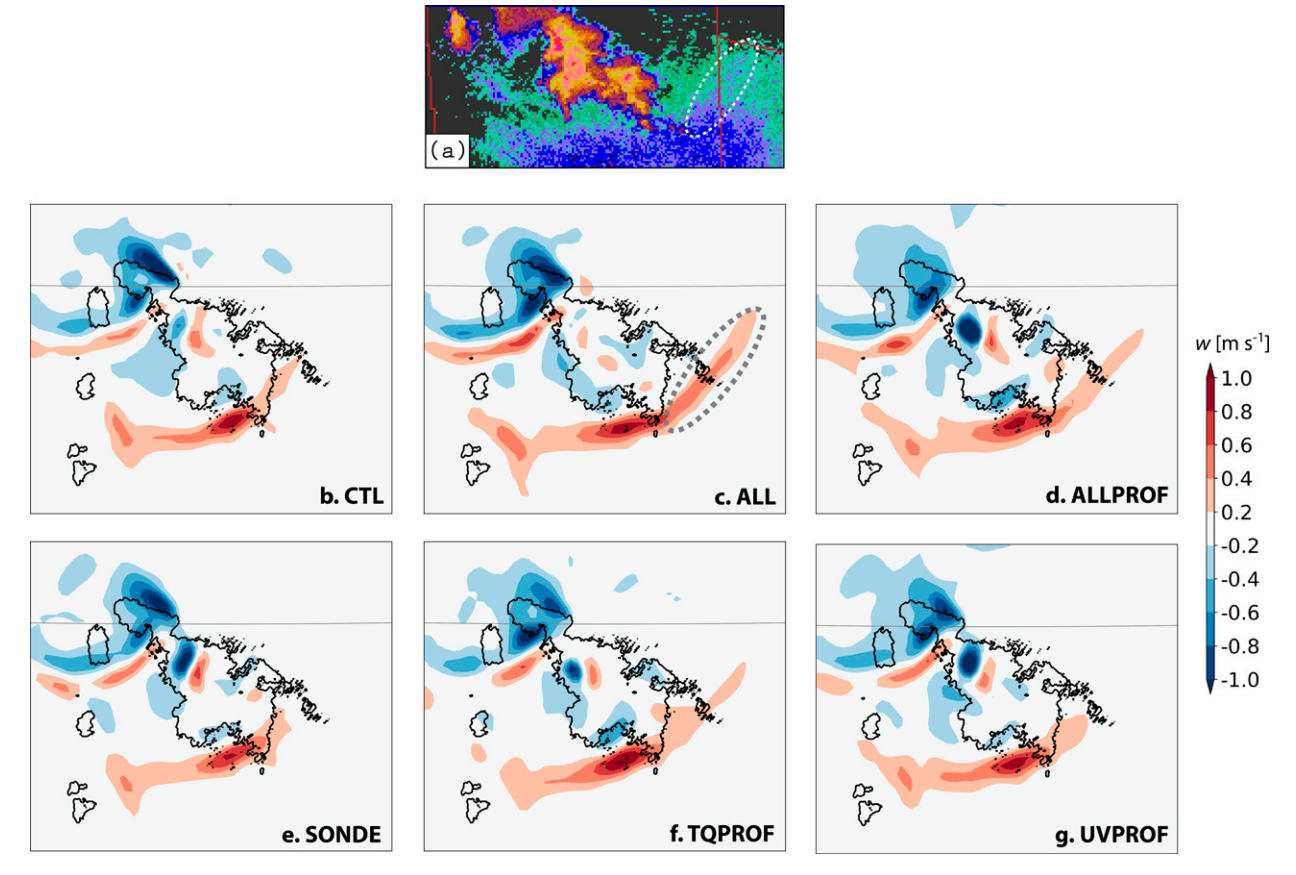


FIG. 6. Example of how the assimilation of different ground-based profiling networks affected the predicted bore extent during the 5 July 2015 case. (a) Observed low-level reflectivity mosaic at 0554 UTC (taken from the PECAN field catalog). (b)–(g) Analysis mean vertical velocity at 1 km AGL (w; color shading) and 30-dBZ composite MRMS reflectivity (black contours) at 0600 UTC. The dashed ellipses in (a) and (c) mark the location of the eastern bore segment discussed in the main text.

impacts in this predictability regime (see Fig. 5a). The same 11 July case was also the focus of a recently published work by Carroll et al. (2021) who leveraged lidar observations and Rapid Refresh model analyses to study the mesoscale moisture transport responsible for the parent MCS initiation on this date.

Figure 9 shows the forecast performance at 0700 UTC—the time when the experimental differences reached their peak values. The low NEPs that the CTL experiment predicted inside the parent MCS are a sign of rapid convective dissipation, which was quite a common feature in this predictability regime. Based on the FSS values in the upper left corner of each panel, it is clear that the most significant gains in forecast skill came from ALL and TQPROF, despite the tendency of these experiments to generate regions of spurious convection to the east of the parent MCS.⁴ Slight improvements can be also seen in ALLPROF, whereas the assimilation of SONDE and UVPROF produced a marginal forecast degradation.

The green scatter dots in Figs. 9b-f represent regions in the model domain where the assimilated ground-based profiling networks caused an increase in the forecasted low-level moisture. They indicate that the aforementioned convective impacts were correlated with differences in the low-level moisture field. More specifically, it appears that the continuous assimilation of the thermodynamic AERI retrievals resulted in a significant moisture increase that maintained the MCS for a longer time. The magnitude of these moisture changes was slightly reduced with the addition of kinematic profilers (see ALLPROF in Fig. 9c), but subsequently increased when all PECAN instruments were assimilated together (see ALL in Fig. 9b). To gain further insights into these results, an additional experiment termed ALLTQ was conducted where only thermodynamic data (in situ and remotely sensed) were assimilated. ALLTQ produced the highest FSSs among all experiments (not shown), implying that the forecast improvements in ALL were caused by the assimilated thermodynamic observations. This enhanced forecast sensitivity to the initial moisture fields aligns well with the findings of Carroll et al. (2021), where it was shown that the convection initiation on 11 July was coincident with an observed maximum in the water vapor flux.

⁴ Additional tests showed that including the region of spurious convection in the FSS calculations did not change the fact that ALL and TQPROF were the best performing experiments in this case.

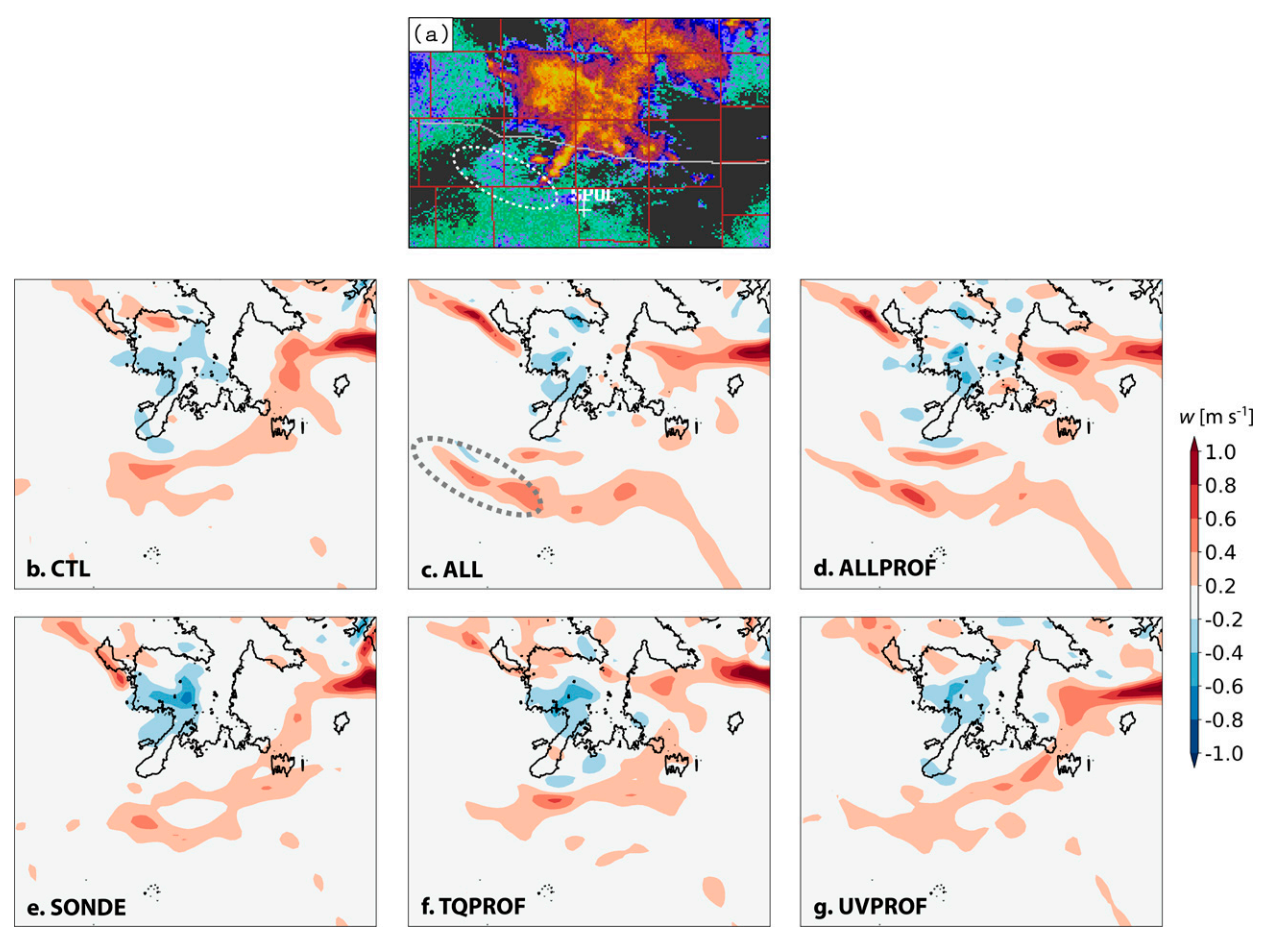


FIG. 7. As in Fig. 6, but with respect to the propagation direction of the explicitly resolved bore during the 5 Jun 2015 case. Both observed and forecasted data are displayed at 0530 UTC on that day.

Although both AERIs and radiosondes provided valuable moisture information that was crucial for the accurate simulation of the bore-generating MCS, the positive moisture differences created by the former experiment were significantly larger. To explain why, we now discuss the low-level moisture innovations at the FP3 PECAN site (see Fig. 10). Focusing on the two solid curves, we first observe that the TQPROF background was consistently drier than the observations following cycle 23. However, the frequent assimilation of AERI retrievals continuously nudged the TQPROF forecasts toward the observed state such that the moisture innovations during the last EnKF cycle became negligible. During cycle 24, the SONDE innovations were also negative and similar in magnitude to TQPROF. Nevertheless, due to the complete lack of observations in subsequent cycles, the background innovations continued to grow and reached 2 g kg⁻¹ during the final analysis time - values that resemble the Rapid Refresh model analysis errors reported in Carroll et al. (2021). At this point, even though the assimilation of FP3 radiosonde data produced large moisture increments, the SONDE analysis innovations remained strongly negative. These diagnostics suggest that the lack of appreciable moisture changes in

SONDE was caused by the small number of PBL observations, which were not able to effectively suppress the growing background errors in this experiment.

To illustrate the forecast degradation in UVPROF, we compared its DA performance to that of TQPROF at 0600 UTC (Fig. 11). During this last EnKF cycle, the low-level moisture background in both experiments contained a localized region of dry air ahead of the parent MCS. Assimilating the MP1 AERI instrument, which was located within the dry region, generated positive increments in water vapor mixing ratio (red contours in Fig. 11a). By contrast, the MP1 kinematic profiler further enhanced the strength of the dry region. To explain these opposite impacts, we need to first recall that qis not a directly observed variable in UVPROF, meaning that all moisture corrections in this experiment were entirely determined by the empirical background covariances. And since q represents a passive tracer in the absence of evaporation or condensation processes, the moisture-wind background covariances in UVPROF reflect the advection of q by the wind. With this in mind, we now observe that the MP1 kinematic profiler induced a westerly wind increment (eastward-pointing black arrows in Fig. 11b) that acted upon a

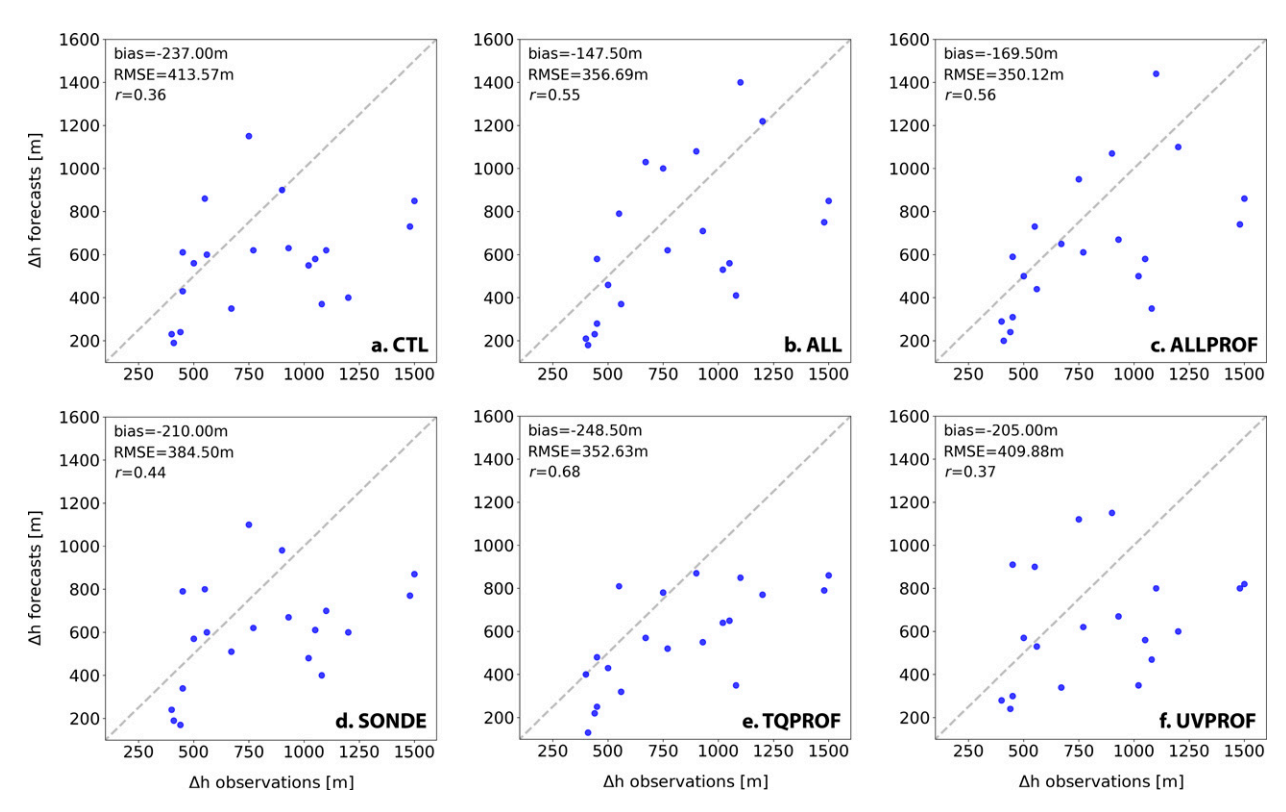


FIG. 8. Systematic verification of the forecasted bore lifting (Δh) . The bias, root-mean-square error (RMSE), and Pearson correlation coefficient (r) associated with different experiments are summarized in the top-left corner of each panel.

sharp moisture gradient around the MP1 site. Since q was considerably smaller upstream of MP1, an increase in the westerly component of the wind was correlated with a decrease in the moisture content.

b. High predictability case: 2 July 2015

The observation impacts in the HP category are exemplified through the 2 July case, which was characterized by a quickly moving MCS with a large, eastward propagating bore. As expected, CTL produced a very satisfactory prediction of the parent MCS even 3h into the forecast (Fig. 12a), despite the fact that the total DA period in this HP case was half as large compared to its LP counterpart.

The main motivation for selecting the 2 July event was the superior performance of UVPROF (cf. NEP changes in Fig. 12f)—a typical characteristic in this HP category. Unlike the 11 July case, the convective forecasts here were most sensitive to differences in the forecasted low-level wind field. In particular, the black arrow in Fig. 12f indicates that UVPROF predicted a stronger inflow toward the parent MCS. To reveal how these wind changes affected the subsequent convective evolution, we examined the vertical structure of the simulated cold pools. The cross sections in Fig. 13 show that the stronger inflow in UVPROF enhanced the low-level convergence along the cold pool's leading edge. The associated stronger updraft promoted a more sustained growth of new convective cells, largely alleviating the premature MCS dissipation in CTL. Interestingly, slight increases in the updraft's strength were also observed in the other

PECAN experiments, especially ALLPROF and ALL. Despite their opposite near-surface wind impacts, these two experiments were still able to deepen the cold pool's inflow region and increase the height-integrated convergence along the cold pool's leading edge.

Similar to the LP analysis, we now seek to understand why the kinematic remote sensors were more effective at improving the forecast skill than the corresponding radiosonde instruments. To answer this question, we consider innovation statistics from the FP3 site where most of the forecasted inflow differences in UVPROF originated from. It is clear from Fig. 14a that the wind innovations in UVPROF became negligible after the first EnKF cycle (cf. the solid and dashed blue lines). The small UVPROF increments throughout most of the cycling period suggest that the high observation frequency of the kinematic remote sensor was not an essential ingredient for improving the forecast skill in this case. Instead, it was the ability of UVPROF to correct the model state early enough in the DA window so that the resulting wind changes can affect the subsequent convective evolution.⁵ While this reduced sensitivity to temporal frequency makes radiosondes a potentially useful observing platform, the FP3 crew launched their first weather balloon only during the last

⁵ It could be also argued that the increased sampling frequency of the kinematic remote sensor represents an indirect benefit since it ensures that observations will be made at dynamically important times.

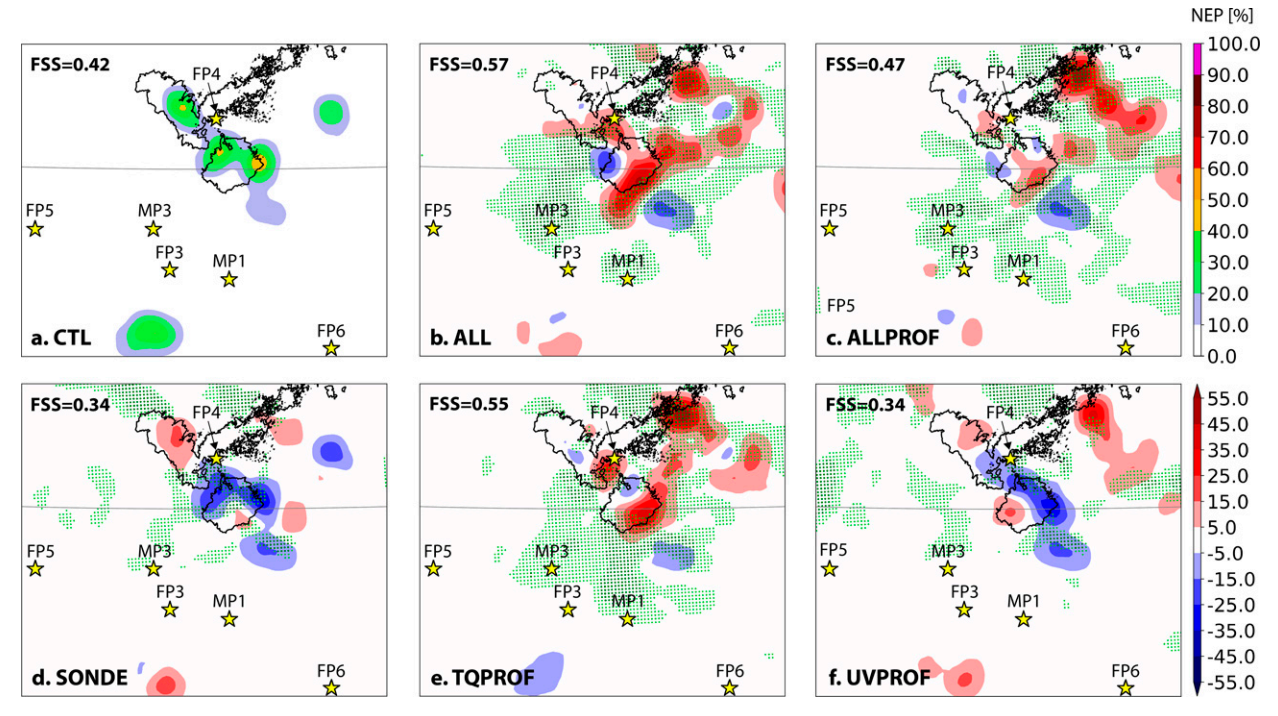


FIG. 9. Convective forecasts for the 11 Jul 2015 case, valid at 0700 UTC (corresponding to a 1-h forecast lead time). The color shading represents (a) the NEP values associated with CTL and (b)–(f) the NEP differences between a given PECAN experiment and CTL. Overlaid on these plots are also the 30-dBZ composite MRMS reflectivity (solid black contours), the experimental differences in the ensemble mean of water vapor mixing ratio at 500 m above the ground (Δq ; light and dark green dots correspond to areas where Δq exceeds 0.5 and 1 g kg⁻¹, respectively), and the position of assimilated ground-based PISA sites (yellow stars). The FSSs associated with each experiment are additionally shown in the top-left corner of each panel. As explained in the main text, the FSS verification subdomain is centered over the parent MCSs and includes the outward-propagating bores.

EnKF cycle, not leaving sufficient time for the wind corrections to be advected toward the cold pool. In fact, comparison between the solid red and blue curves in Fig. 14a indicates that the initial wind errors at FP3 amplified over the cycling period and created an even greater observation misfit during SONDE's first assimilation time.

The inability of TQPROF to create meaningful wind increments in this HP case can be primarily attributed to the high accuracy of the background low-level moisture fields (relative

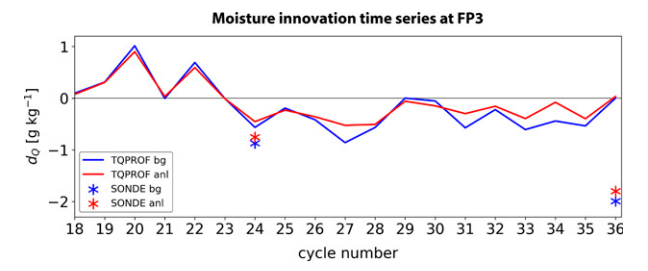


FIG. 10. FP3 innovation time series of specific humidity (d_Q) averaged over the 950–850-hPa layer and shown for the second half of the 6-h EnKF cycling period on 11 Jul 2015. Note that the innovation values plotted here represent the ensemble mean minus observation differences; the blue and red colors refer to the background (bg) and analysis (anl) innovations, respectively.

to the LP case), as evidenced by the root-mean-square innovation (RMSI) profiles in Fig. 14b. To be more precise, the absence of large moisture innovations prevented the EnKF from making significant changes to both observed and unobserved state variables. Further diagnostics also revealed that the small moisture innovations in TQPROF were accompanied by relatively small moisture–wind correlations. As a result, even the few EnKF cycles that featured relatively large moisture corrections were not able to produce sizeable wind increments.

c. Medium predictability case: 5 June 2015

We close this Section by discussing the forecast impacts the 5 June case when the convective evolution was considerably more complex in comparison to the previous two cases. The bore-generating MCS here interacted with another, much larger MCS to its northeast (see the upper-right corner of Fig. 15a). Problems with the CTL experiment included the low NEP values inside the parent MCS as well as the simulation of spurious NEP probabilities to its east. Consistent with our conclusions for the MP category, forecast improvements in this case required the simultaneous assimilation of thermodynamic and kinematic profilers (Fig. 15c). By contrast, the use of networks consisting of single remote sensors resulted in either neutral or slightly negative impacts, primarily due to further NEP reductions inside the parent MCS (Figs. 15e,f).

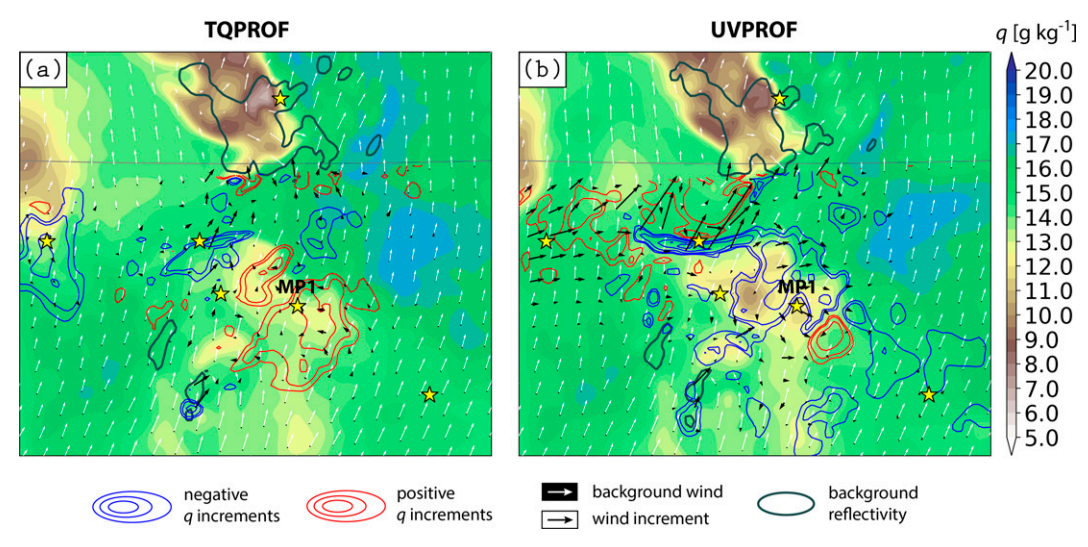


FIG. 11. Comparing the 500 m AGL analysis increments in (a) TQPROF and (b) UVPROF during the last EnKF cycle on 11 Jul 2015 (valid at 0600 UTC). The color shading, white arrows, and solid dark gray contours represent the background ensemble means of water vapor mixing ratio (q), wind, and 30-dBZ reflectivity, respectively. Positive (negative) q increments are shown as red (blue) contours and are displayed for the following values: ± 0.15 , ± 0.25 , ± 0.5 , ± 1 , ± 1.5 , ± 2 , and ± 2.5 g kg⁻¹. Wind increments are shown as black arrows and are additionally magnified ~10.6 times relative to the background wind. Note that the moisture and wind increments inside the parent MCS are deliberately clipped in order to better highlight the environmental changes brought by the assimilated ground-based remote sensors (see yellow stars).

The location of the FP3 site (see yellow star in Fig. 16a), which was assimilated as part of our 5 June experiments, partly explains why it was necessary to observe both the thermodynamic and kinematic components of the model state: it was positioned very close to a sharp near-surface boundary

characterized by strong variations in moisture and wind (and along which the bore-generating convective system developed in later EnKF cycles).

Given that SONDE was the best performing single profiler experiment during this case, we now examine its low-level

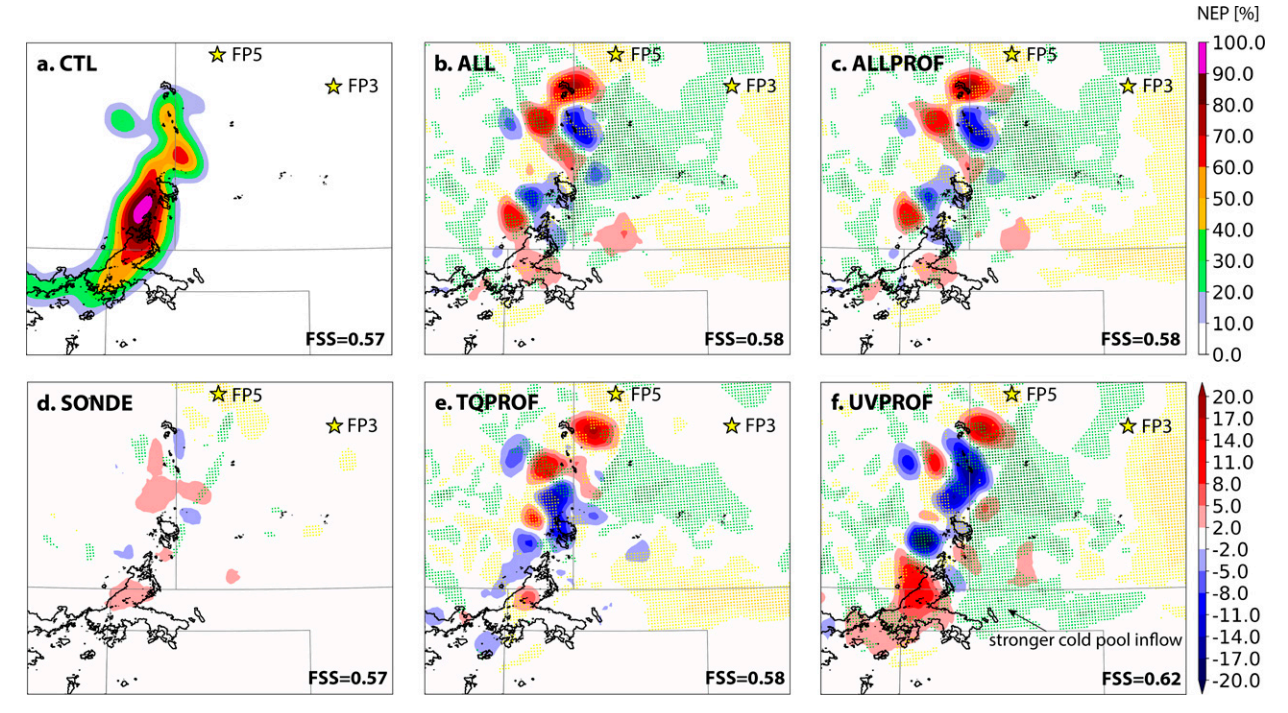


FIG. 12. As in Fig. 9, but for 0600 UTC 2 Jul 2015 (corresponding to a 3-h forecast lead time). The green (yellow) dots show negative (positive) differences in the u component of the ensemble-mean wind at 500 m AGL; the lighter (darker) colors mark regions where these differences exceed 0.5 (1) m s⁻¹.

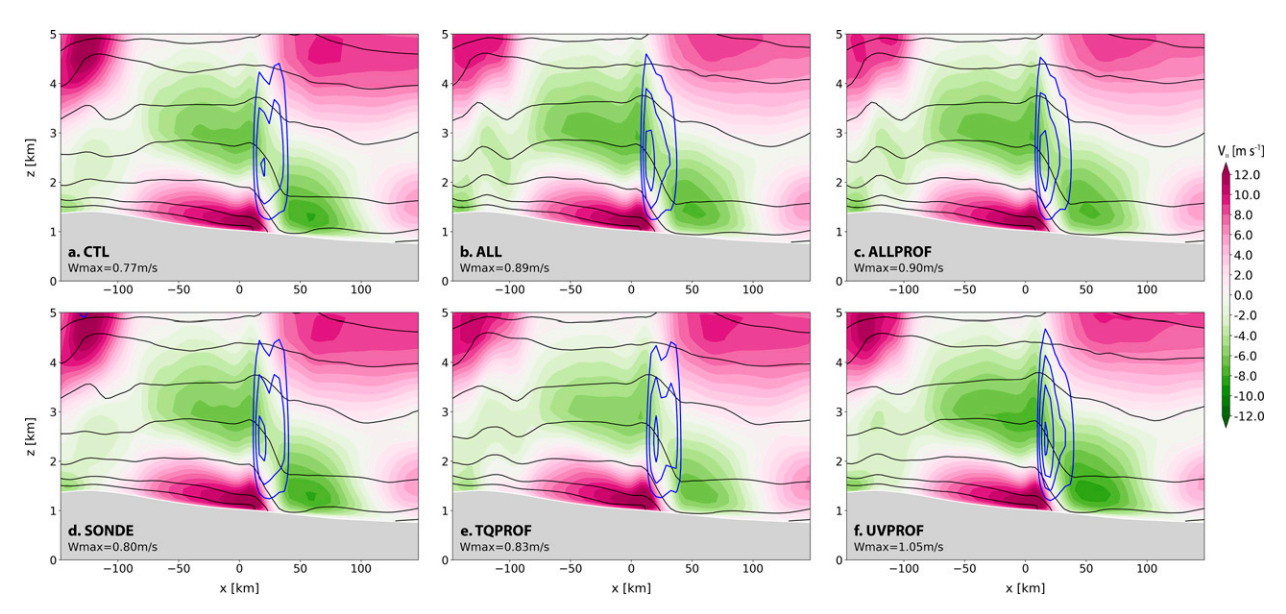


FIG. 13. Vertical cross sections through the cold pool associated with the parent MCS on 2 Jul 2015. The color shading displays the horizontal wind speed parallel to the cross section, with positive (negative) values indicating flow oriented in the positive (negative) x direction. The solid black contours show the virtual potential temperature and are plotted every 2 K, starting from 310 K near the surface. Vertical velocities are also shown as solid blue contours whose spacing and initial value are both set to 0.25 m s⁻¹. The maximum value of the vertical velocity (Wmax) is additionally labeled in the bottom-left corner of each panel. All cross sections are valid at 0530 UTC, which corresponds to a 2.5-h forecast lead time for this PECAN case.

increments (overlaid in Fig. 16a) in order to justify some of the subsequent forecast improvements. Evidently, the dry moisture increments at 500 m AGL extended to 2 km AGL (Fig. 16b) where the background wind was oriented from south-southwest. The resulting negative SONDE-CTL moisture differences were then advected into the region of spurious convection and

helped suppress the excessively large NEP values in CTL. Insofar as the wind impacts in SONDE are concerned, the black arrows in Fig. 16a reveal two main types of corrections. The first one pertains to a broad area of southerly wind increments around the FP3 site that reflects an underestimation in the forecasted LLJ speed. We also observe

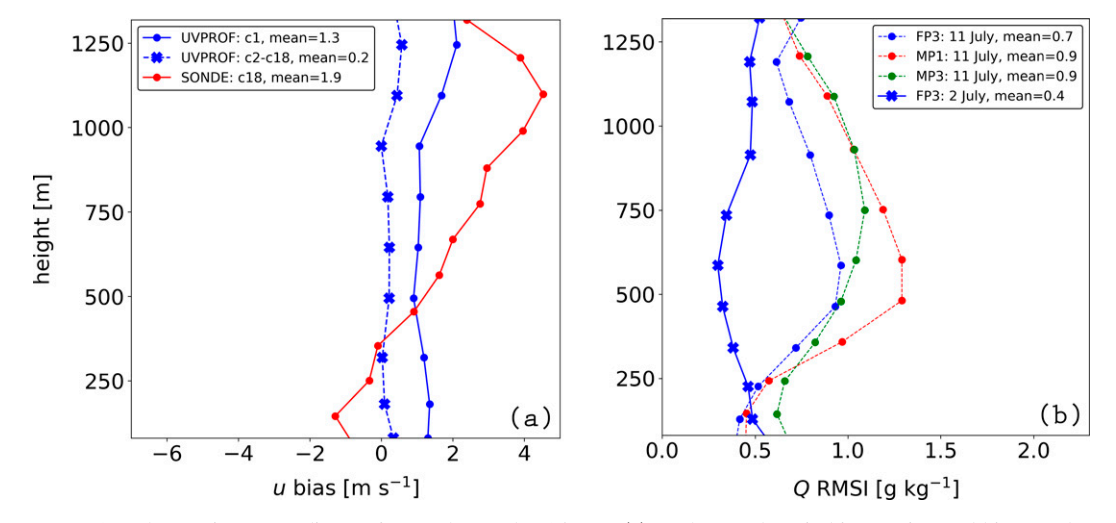


FIG. 14. Observation space diagnostics for the 2 Jul 2015 case. (a) Background *u*-wind innovation and bias profiles (solid and dashed curves, respectively) for UVPROF and SONDE (blue and red colors, respectively) at the FP3 site. Note that the UVPROF's bias profile represents an average over all UVPROF's innovations between the 2nd and 18th cycles. (b) Background root-mean-square innovation (RMSI) profiles of specific humidity (*Q*) associated with TQPROF for the 2 Jul (solid curve) and 11 Jul 2015 (dashed curves) cases. All RMSI profiles are averaged over the last 3 h prior to model initialization.

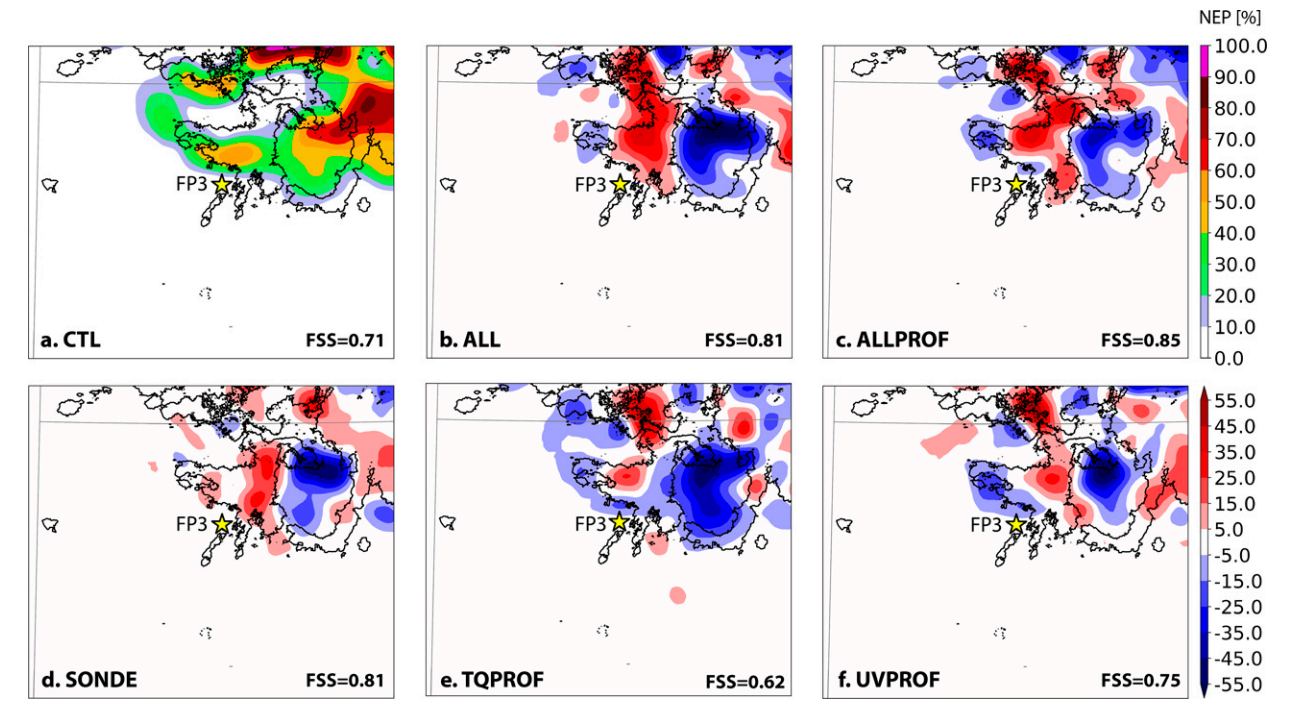


FIG. 15. As in Fig. 9, but for 0600 UTC 5 Jun 2015 (corresponding to a 1.5-h forecast lead time).

northeasterly wind increments between the two convective cells to the northwest of FP3 (see yellow ellipse in Fig. 16a), which were induced by the spatial wind covariances in the background ensemble. Regardless of their origin, the effect of both increment types was to strengthen the preexisting low-level convergence to the north of FP3. Somewhat analogous to the dynamical mechanisms discussed as part of the HP case, the resulting enhancement of the low-level vertical velocity (see red contours in Fig. 16c) created more favorable conditions for convective growth and likely explains why SONDE predicted higher NEP values inside the parent MCS.

Next, to understand why the TQPROF and UVPROF predictions were not as skillful, we examine their DA impacts during two different EnKF cycles. The first one is valid at 0310 UTC (first row of Fig. 17), i.e., only 10 min after assimilating the FP3 radiosonde observations. Although the increments in TQPROF and UVPROF were not as coherent or widespread as those in SONDE, they appear to be subjectively consistent - both in terms of the reduced moisture content as well as the strengthened LLJ. This similarity between TQPROF and UVPROF, which occurred during several other EnKF cycles, comes in contrast to the LP case where the two experiments produced opposite increments. To explain this apparent discrepancy, we note that the low-level moisture on 5 June 2015 varied on much larger scales compared to the LP case and was also strongly correlated with the low-level wind field. For example, the dry air mass was clearly associated with south-southwesterly winds, whereas the flow in the moist air mass had a predominantly easterly component. In this much simpler dynamical context, measurements of either moisture or wind are sufficient to accurately constrain both variables during the EnKF analysis update.

The aforementioned dynamical situation changed during the last hour of EnKF cycling when convection started to develop over the FP3 site. As a result of the highly nonlinear convective dynamics, the wind-moisture relationship became more complex and it was no longer possible to accurately estimate the model state by only assimilating single remote sensors. This effect is illustrated well on the bottom row of Fig. 17: we see that TQPROF produced a distinctly negative moisture increment around FP3, whereas the moisture changes in UVPROF were more or less neutral despite the much larger background moisture content in UVPROF. We hypothesize it was, namely, these cross-variable analysis errors that eventually degraded the TQPROF and UVPROF performance.

Finally, it is worth remarking that the strategic timing of the FP3 radiosonde launch likely enhanced the overall forecast benefits in SONDE. Specifically, the FP3 radiosonde provided vital environmental information just prior to convection initiation when the relatively linear model dynamics still enabled the EnKF algorithm to generate meaningful PBL corrections. This setup is to be contrasted with the HP case where the lack of radiosonde measurements early in the DA window limited their subsequent impacts.

6. Summary and conclusions

This work evaluated the benefits of various ground-based profiling networks across 10 diverse cases from the Plains Elevated Convection at Night (PECAN) field campaign. In particular, we explored the impacts of assimilating in situ and remote sensing instruments on the short-range forecasts of bore-generating nocturnal convection. A total of five data addition experiments were

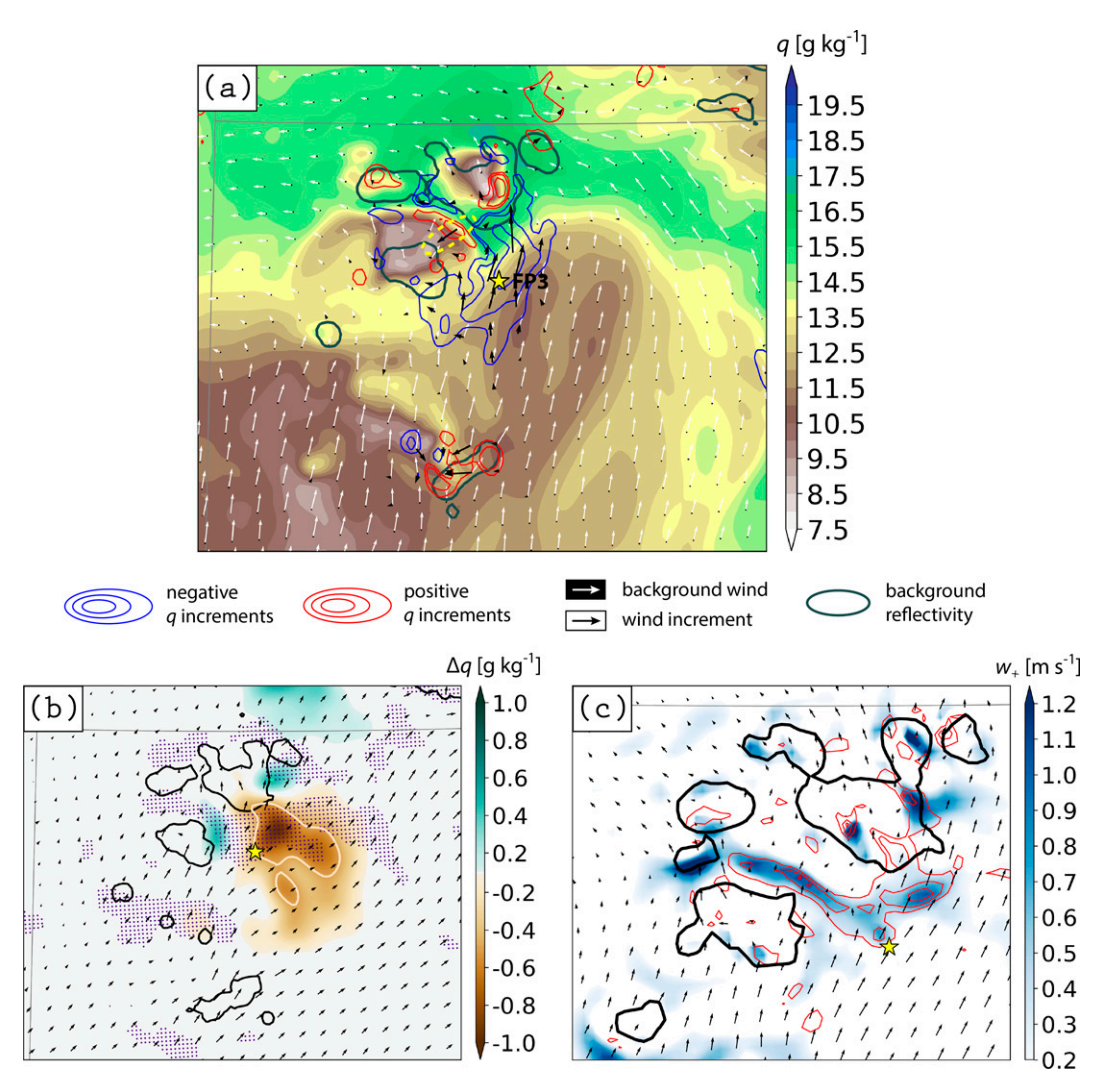


FIG. 16. Dynamical interpretation of the forecast improvements during the 5 Jun 2015 case. (a) Analysis increments for SONDE at 0300 UTC. The meaning of all symbols is as in Fig. 11, but that the q increments are drawn at ± 0.5 , ± 0.1 , ± 2 , and ± 4 g kg $^{-1}$, whereas the ratio of background to increment wind (represented by the white and black arrows, respectively) is \sim 1:3. The dashed yellow ellipse shows the position of the northeasterly wind increment discussed in the main text. (b) SONDE-CTL analysis mean q differences (Δq ; color shading) at 2 km AGL and valid at 0300 UTC. Regions where Δq is equal to -0.5 g kg $^{-1}$ are highlighted with bisque contours. The solid black contours and black arrows represent SONDE's analysis mean of 30-dBZ reflectivity and wind at 2 km AGL, respectively, while the purple dots indicate grid points where the analysis mean vertical velocity at 1 km AGL exceeds 0.15 m s $^{-1}$. (c) SONDE's analysis mean updraft strength at 1 km AGL (w_+ ; blue shading) and its change relative to CTL (red contours starting at 0.1 m s $^{-1}$ and plotted every 0.2 m s $^{-1}$) at 0310 UTC. The solid black contours and black arrows have the same meaning as in (b), but are shown for 1 km AGL. Finally, the position of the FP3 site is marked with a yellow star in all panels.

conducted in order to evaluate the relative merits of networks with single and combined instrument designs.

Aggregated verification statistics revealed that the largest forecast improvements are obtained by simultaneously assimilating in situ and remote sensing profilers. Combining thermodynamic and kinematic remote sensors also resulted in measurable benefits, especially with respect to the explicitly resolved bores. On the other hand, the average impacts from single profiler networks were shown to be mostly neutral in sign. Detailed analysis revealed that the lack of statistically

detectable benefits from such networks is related to their flow-dependent performance: thermodynamic and kinematic remote sensors were found to be most beneficial in cases with low and high convective skill, respectively. When averaged across the 10 cases, these variable impacts negated each other, explaining why the skill of single profiler experiments was not statistically different from our control simulations.

To illustrate the aforementioned sensitivities, we used three representative cases and showed that the underlying dynamical context plays a crucial role in shaping the forecast impacts from

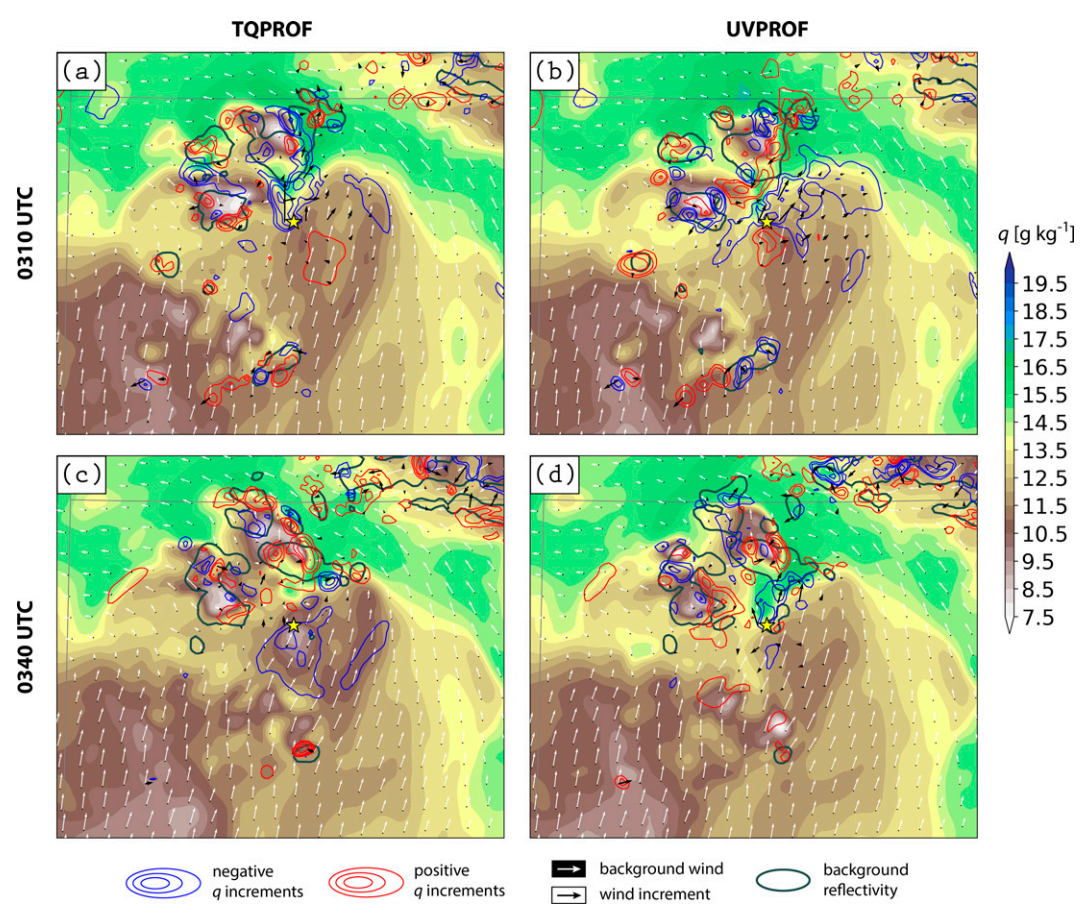


FIG. 17. Comparing the low-level analysis increments in TQPROF and UVPROF during two EnKF cycles on 5 Jun 2015: (top) before and (bottom) after the initiation of convection over the FP3 site. The data shown in these panels are as in Fig. 16a, but the ratio of background to increment wind (white and black arrows, respectively) here is \sim 2:5 and the \pm 0.25 g kg⁻¹ q increment is additionally plotted.

different ground-based profiling networks. Our examination of the low predictability case, for instance, uncovered that the evolution of the bore-generating convective system is sensitive to both the low-level moisture analysis and the frequency of moisture observations, in turn justifying the better forecast performance caused by the assimilation of thermodynamic remote sensors. By contrast, the positive impact of kinematic profilers during the high predictability case were linked to an enhanced forecast sensitivity to the low-level wind field.

Our study also demonstrated that the performance of single profiling networks is contingent upon limitations in the underlying DA methodology. This is due to the fact that accurately estimating the unobserved portion of the model state is closely related to the quality of the background error covariances. The main advantage of the EnKF approach used here is that it provides a flow-dependent covariance estimate based only on a small number of ensemble members. In the special case of quasi-linear model dynamics and comparable variability in the moisture and wind fields (Figs. 17a,b), we found that the ensemble-based covariances are sufficiently accurate to allow single profiler networks to introduce physically sound corrections with respect to both mass and wind variables.

On the contrary, when the flow was governed by highly nonlinear dynamics (Figs. 17c,d) and/or the background moisture varied on scales much smaller than the corresponding wind field (Fig. 11), a simultaneous estimation of the thermodynamic and kinematic PBL properties was no longer possible. In these situations, the ensemble-based covariances could not faithfully describe the true wind-moisture relationship - either as a direct consequence of the more complicated dynamics or due to the insufficient number of ensemble members needed to accurately resolve the small-scale moisture variability. Consequently, errors in the analysis of unobserved state variables accumulated over time and had an adverse impact on the forecasts. All in all, these findings suggest that the spatiotemporal characteristics of the lowlevel moisture transport—an archetypal feature of the nocturnal environment over the Great Plains (Trier and Parsons 1993; Trier et al. 2017; Hitchcock et al. 2019; Weckwerth and Romatschke 2019), have important consequences on our ability to extract meaningful information from single remote sensing networks.

Undoubtedly, future developments in DA theory would be vital for the better utilization of ground-based remote sensing technology. One possible research direction involves the development of novel methods for estimating the optimal observation error statistics. The high vertical resolution and temporal frequency of some remote sensors, such as the AERI, make it necessary to introduce spatial and temporal correlations in the error covariance matrices. Recent findings from Degelia and Wang (2021, manuscript submitted to Mon. Wea. Rev.) have also demonstrated that convective forecasts can be further improved by adopting a flow-dependent treatment of the observation error statistics. Another interesting line of future research would be to explore the benefits of directly assimilating the raw remote sensing measurements (as opposed to having to rely on a separate retrieval algorithm). Such an idea is highly appealing as it would allow for a more straightforward quantification of the measurement uncertainties in the estimation process. Finally, the contrasting moisture variability in our cases would naturally benefit from a multiscale DA approach capable of imposing different correlation structures as a function of the analyzed scales (e.g., Wang et al. 2021).

We would like to conclude this article by recognizing that the relative importance of different initial-condition variables in the three predictability categories might be an artifact of our case selection. In other words, there may be other situations where the forecast skill in low (high)-predictability regimes is more sensitive to the initial wind (moisture) fields, which would act to reverse the impacts reported in our single profiler experiments. A better understanding of which initial state variables have the largest impact on the subsequent forecast errors is essential for designing new observing systems.

Acknowledgments. This work was primarily funded through NSF Award AGS-1359703. The involvement of one of the investigators (David B. Parsons) was in part supported by NSF Award AGS-1921587. Computing resources were provided by the Extreme Science and Engineering Discovery Environment (XSEDE), which is supported by National Science Foundation Grant ACI-1548562. The authors thank Alan Shapiro and Evgeni Fedorovich for useful discussions on some dynamical aspects pertaining to bore-generating nocturnal convection. Ross Bannister is acknowledged for providing valuable insights on how moisture-wind correlations are treated in operational DA systems. We also extend our gratitude to Patrick Calhoun, David Akin, and Horst Severini from OU Supercomputing Center for Education and Research (OSCER) for their technical support with the PetaStore system. Finally, we appreciate the constructive feedback of three anonymous reviewers on earlier versions of this manuscript. The National Center for Atmospheric Research is sponsored by the National Science Foundation.

Data availability statement. The data from our numerical experiments are archived locally and available upon request.

REFERENCES

Adam, S., A. Behrendt, T. Schwitalla, E. Hammann, and V. Wulfmeyer, 2016: First assimilation of temperature lidar data into an NWP model: Impact on the simulation of the temperature field, inversion strength and PBL depth. Quart.

- J. Roy. Meteor. Soc., 142, 2882–2896, https://doi.org/10.1002/qj. 2875
- Benjamin, S. G., B. E. Schwartz, E. J. Szoke, and S. E. Koch, 2004: The value of wind profiler data in U. S. weather forecasting. *Bull. Amer. Meteor. Soc.*, 85, 1871–1886, https://doi. org/10.1175/BAMS-85-12-1871.
- Bouttier, F., 2001: The use of profiler data at ECMWF. *Meteor. Z.*, **10**, 497–510, https://doi.org/10.1127/0941-2948/2001/0010-0497.
- Carroll, B. J., B. B. Demoz, D. D. Turner, and R. Delgado, 2021: Lidar observations of a mesoscale moisture transport event impacting convection and comparison to Rapid Refresh model analysis. *Mon. Wea. Rev.*, 149, 463–477, https://doi.org/ 10.1175/MWR-D-20-0151.1.
- Caumont, O., and Coauthors, 2016: Assimilation of humidity and temperature observations retrieved from ground-based microwave radiometers into a convective-scale NWP model. *Quart. J. Roy. Meteor. Soc.*, 142, 2692–2704, https://doi.org/ 10.1002/qj.2860.
- Chipilski, H. G., X. Wang, and D. B. Parsons, 2018: Object-based algorithm for the identification and tracking of convective outflow boundaries in numerical models. *Mon. Wea. Rev.*, 146, 4179–4200, https://doi.org/10.1175/MWR-D-18-0116.1.
- —, and —, 2020: Impact of assimilating PECAN profilers on the prediction of bore-driven nocturnal convection: A multi-scale forecast evaluation for the 6 July 2015 case study. *Mon. Wea. Rev.*, **148**, 1147–1175, https://doi.org/10.1175/MWR-D-19-0171.1.
- Chou, M.-D., and M. J. Suarez, 1994: An efficient thermal infrared radiation parameterization for use in general circulation models. NASA Tech. Memo. 104606, Vol. 3, NASA/Goddard Space Flight Center, 85 pp.
- Coniglio, M. C., G. S. Romine, D. D. Turner, and R. D. Torn, 2019: Impacts of targeted AERI and Doppler lidar wind retrievals on short-term forecasts of the initiation and early evolution of thunderstorms. *Mon. Wea. Rev.*, **147**, 1149–1170, https://doi.org/10.1175/MWR-D-18-0351.1.
- Crook, N. A., 1996: Sensitivity of moist convection forced by boundary layer processes to low-level thermodynamic fields. *Mon. Wea. Rev.*, 124, 1767–1785, https://doi.org/10.1175/1520-0493(1996)124<1767:SOMCFB>2.0.CO;2.
- Degelia, S. K., X. Wang, D. Stensrud, and D. D. Turner, 2020: Systematic evaluation of the impact of assimilating a network of ground-based remote sensing profilers for forecasts of nocturnal convection initiation during PECAN. Mon. Wea. Rev., 148, 4703–4728, https://doi.org/10.1175/MWR-D-20-0118.1.
- Fourriè, N., M. Nuret, P. Brousseau, and O. Caumont, 2021: Data assimilation impact studies with the AROME-WMED reanalysis of the first special observation period of the Hydrological cycle in the Mediterranean Experiment. *Nat. Hazards Earth* Syst. Sci., 21, 463–480, https://doi.org/10.5194/nhess-21-463-2021.
- Geerts, B., and Coauthors, 2017: The 2015 Plains Elevated Convection at Night field project. *Bull. Amer. Meteor. Soc.*, 98, 767–786, https://doi.org/10.1175/BAMS-D-15-00257.1.
- Grell, G. A., and D. Devenyi, 2002: A generalized approach to parameterizing convection combining ensemble and data assimilation techniques. *Geophys. Res. Lett.*, 29, 1693, https:// doi.org/10.1029/2002GL015311.
- —, and S. R. Freitas, 2014: A scale and aerosol aware stochastic convective parameterization for weather and air quality modeling. *Atmos. Chem. Phys.*, 14, 5233–5250, https://doi.org/ 10.5194/acp-14-5233-2014.
- Grzeschik, M., and Coauthors, 2008: Four-dimensional variational data analysis of water vapor Raman lidar data and their

- impact on mesoscale forecasts. *J. Atmos. Oceanic Technol.*, **25**, 1437–1453, https://doi.org/10.1175/2007JTECHA974.1.
- Gustafsson, N., and Coauthors, 2018: Survey of data assimilation methods for convective-scale numerical weather prediction at operational centres. *Quart. J. Roy. Meteor. Soc.*, 144, 1218–1256, https://doi.org/10.1002/qj.3179.
- Haghi, K. R., D. B. Parsons, and A. Shapiro, 2017: Bores observed during IHOP_2002: The relationship of bores to the nocturnal environment. *Mon. Wea. Rev.*, 145, 3929–3946, https://doi.org/10.1175/MWR-D-16-0415.1.
- —, and Coauthors, 2018: Bore-ing into nocturnal convection. *Bull. Amer. Meteor. Soc.*, **100**, 1103–1121, https://doi.org/10.1175/BAMS-D-17-0250.1.
- Hitchcock, S. M., R. S. Schumacher, G. Herman, M. C. Coniglio, M. D. Parker, and C. L. Ziegler, 2019: Evolution of pre- and postconvective environmental profiles from mesoscale convective systems during PECAN. *Mon. Wea. Rev.*, 147, 2329–2354, https://doi.org/10.1175/MWR-D-18-0231.1.
- Hong, S., and J. J. Lim, 2006: TheWRF single-moment 6-class microphysics scheme (WSM6). J. Korean Meteor. Soc., 42, 129–151.
- Hu, J., N. Yussouf, D. D. Turner, T. A. Jones, and X. Wang, 2019: Impact of ground-based remote sensing boundary layer observations on short-term probabilistic forecasts of a tornadic supercell event. Wea. Forecasting, 34, 1453–1476, https://doi.org/10.1175/WAF-D-18-0200.1.
- Iacono, M. J., J. S. Delamere, E. J. Mlawer, M. W. Shephard, S. A. Clough, and W. D. Collins, 2008: Radiative forcing by long-lived greenhouse gases: Calculations with the AER radiative transfer models. J. Geophys. Res., 113, D13103, https:// doi.org/10.1029/2008JD009944.
- Johnson, A., and X. Wang, 2019: Multicase assessment of the impacts of horizontal and vertical grid spacing, and turbulence closure model, on subkilometer-scale simulations of atmospheric bores during PECAN. *Mon. Wea. Rev.*, 147, 1533–1555, https://doi.org/10.1175/MWR-D-18-0322.1.
- —, —, J. R. Carley, L. J. Wicker, and C. Karstens, 2015: A comparison of multiscale GSI-based EnKF and 3DVar data assimilation using radar and conventional observations for midlatitude convective-scale precipitation forecasts. *Mon. Wea. Rev.*, 143, 3087–3108, https://doi.org/10.1175/MWR-D-14-00345.1.
- —, K. R. Haghi, and D. B. Parsons, 2018: Evaluation of forecasts of a convectively generated bore using an intensively observed case study from PECAN. *Mon. Wea. Rev.*, 146, 3097–3122, https://doi.org/10.1175/MWR-D-18-0059.1.
- Kain, J. S., 2004: The Kain–Fritsch convective parameterization: An update. *J. Appl. Meteor.*, **43**, 170–181, https://doi.org/10.1175/1520-0450(2004)043<0170:TKCPAU>2.0.CO;2.
- Kawabata, T., H. Iwai, H. Seko, Y. Shoji, K. Saito, S. Ishii, and K. Mizutani, 2014: Cloud-resolving 4D-Var assimilation of Doppler wind lidar data on a meso-gamma-scale convective system. Mon. Wea. Rev., 142, 4484–4498, https://doi.org/10.1175/MWR-D-13-00362.1.
- Leuenberger, D., A. Haefele, N. Omanovic, M. Fengler, G. Martucci, B. Calpini, O. Fuhrer, and A. Rossa, 2020: Improving high-impact numerical weather prediction with lidar and drone observations. *Bull. Amer. Meteor. Soc.*, 101, E1036– E1051, https://doi.org/10.1175/BAMS-D-19-0119.1.
- Lewis, W. E., T. J. Wagner, J. A. Otkin, and T. A. Jones, 2020: Impact of AERI temperature and moisture retrievals on the simulation of a Central Plains severe convective weather event. *Atmosphere*, 11, 729, https://doi.org/10.3390/atmos11070729.

- Li, L., N. Xie, L. Fu, K. Zhang, A. Shao, Y. Yang, and X. Ren, 2020: Impact of lidar data assimilation on low-level wind shear simulation at Lanzhou Zhongchuan international airport, China: A case study. *Atmosphere*, 11, 1342, https://doi. org/10.3390/atmos11121342.
- Lilly, D. K., and D. Perkey, 1976: Sensitivity of mesoscale predictions to mesoscale initial data. *Quart. J. Roy. Meteor. Soc.*, 116, 779–798.
- Lin, G., C. Grasmick, B. Geerts, Z. Wang, and M. Deng, 2021: Convection initiation and bore formation following the collision of mesoscale boundaries over a developing stable boundary layer: A case study from PECAN. *Mon. Wea. Rev.*, 149, 2351–2367, https://doi.org/10.1175/MWR-D-20-0282.1.
- Loveless, D. M., T. J. Wagner, D. D. Turner, S. A. Ackerman, and W. F. Feltz, 2019: A composite perspective on bore passage during the PECAN campaign. *Mon. Wea. Rev.*, 147, 1395–1413, https://doi.org/10.1175/MWR-D-18-0291.1.
- Maddox, R. A., 1980: Mesoscale convective complexes. *Bull. Amer. Meteor. Soc.*, **61**, 1374–1387, https://doi.org/10.1175/1520-0477(1980)061<1374;MCC>2.0.CO;2.
- Martinet, P., A. Dabas, J.-M. Donier, T. Douffet, O. Garrouste, and R. Guillot, 2015: 1D-Var temperature retrievals from microwave radiometer and convective scale model. *Tellus*, 67A, 27925, https://doi.org/10.3402/tellusa.v67.27925.
- —, D. Cimini, F. De Angelis, G. Canut, V. Unger, R. Guillot, D. Tzanos, and A. Paci, 2017: Combining ground-based microwave radiometer and the AROME convective scale model through 1DVar retrievals in complex terrain: An alpine valley case study. *Atmos. Meas. Tech.*, 10, 3385–3402, https://doi.org/10.5194/amt-10-3385-2017.
- Miller, R. L., C. L. Ziegler, and M. I. Biggerstaff, 2020: Seven-Doppler radar and in situ analysis of the 25–26 June 2015 Kansas MCS during PECAN. Mon. Wea. Rev., 148, 211–240, https://doi.org/10.1175/MWR-D-19-0151.1.
- Mueller, D., B. Geerts, Z. Wang, M. Deng, and C. Grasmick, 2017: Evolution and vertical structure of an undular bore observed on 20 June 2015 during PECAN. *Mon. Wea. Rev.*, 145, 3775–3794, https://doi.org/10.1175/MWR-D-16-0305.1.
- Nakanishi, M., and H. Niino, 2006: An improved Mellor–Yamada level-3 model: Its numerical stability and application to a regional prediction of advection fog. *Bound.-Layer Meteor.*, 119, 397–407, https://doi.org/10.1007/s10546-005-9030-8.
- National Research Council, 2009: Observing Weather and Climate from the Ground up: A Nationwide Network of Networks. The National Academies Press, 250 pp., https://doi.org/10. 17226/12540.
- ——, 2010: When Weather Matters: Science and Services to Meet Critical Societal Needs. The National Academies Press, 198 pp., https://doi.org/10.17226/12888.
- ——, 2012: Weather Services for the Nation: Becoming Second to None. The National Academies Press, 86 pp., https://doi.org/ 10.17226/13429.
- Parker, M. D., B. S. Borchardt, R. L. Miller, and C. L. Ziegler, 2020: Simulated evolution and severe wind production by the 25–26 June 2015 nocturnal MCS from PECAN. *Mon. Wea. Rev.*, 148, 183–209, https://doi.org/10.1175/MWR-D-19-0072.1.
- Parsons, D. B., K. R. Haghi, K. T. Halbert, B. Elmer, and J. Wang, 2019: The potential role of atmospheric bores in the initiation and maintenance of nocturnal convection over the southern Great Plains. J. Atmos. Sci., 76, 43–68, https://doi.org/10.1175/ JAS-D-17-0172.1.
- Qi, Y., S. Fan, J. Mao, B. Li, C. Guo, and S. Zhang, 2021: Impact of assimilating ground-based microwave radiometer data on

- the precipitation bifurcation forecast: A case study in Beijing. *Atmosphere*, **12**, 551, https://doi.org/10.3390/atmos12050551.
- Smith, E. N., G. J. Gebauer, P. M. Klein, E. Fedorovich, and J. A. Gibbs, 2019: The Great Plains low-level jet during PECAN: Observed and simulated characteristics. *Mon. Wea. Rev.*, 147, 1845–1869, https://doi.org/10.1175/MWR-D-18-0293.1.
- Stechman, D. M., G. M. McFarquhar, R. M. Rauber, B. F. Jewett, and R. A. Black, 2020: Composite in situ microphysical analysis of all spiral vertical profiles executed within BAMEX and PECAN mesoscale convective systems. *J. Atmos. Sci.*, 77, 2541–2565, https://doi.org/10.1175/JAS-D-19-0317.1.
- Tewari, M., and Coauthors, 2004: Implementation and verification of the unified Noah land surface model in the WRF model. 20th Conf. on Weather Analysis and Forecasting/16th Conf. on Numerical Weather Prediction, Seattle, WA, Amer. Meteor. Soc., 14.2A, https://ams.confex.com/ams/84Annual/webprogram/Paper69061.html.
- Thompson, G., P. R. Field, R. M. Rasmussen, and W. D. Hall, 2008: Explicit forecasts of winter precipitation using an improved bulk microphysics scheme. Part II: Implementation of a new snow parameterization. *Mon. Wea. Rev.*, 136, 5095–5115, https://doi.org/10.1175/2008MWR2387.1.
- Trier, S. B., and D. B. Parsons, 1993: Evolution of environmental conditions preceding the development of a nocturnal mesoscale convective complex. *Mon. Wea. Rev.*, **121**, 1078–1098, https://doi.org/10.1175/1520-0493(1993)121<1078:EOECPT> 2.0 CO:2.
- —, J. W. Wilson, D. A. Ahijevych, and R. A. Sobash, 2017: Mesoscale vertical motions near nocturnal convection initiation in PECAN. *Mon. Wea. Rev.*, **145**, 2919–2941, https://doi. org/10.1175/MWR-D-17-0005.1.
- Vandenberghe, F., and R. Ware, 2002: 4-dimensional variational assimilation of ground-based microwave observations during a winter fog event. *Proc. Int. Symp. on Atmospheric Sensing with GPS*, Tsukuba, Japan, Japan Meteorological Agency, 3–05, https://radiometrics.com/wp-content/uploads/2021/10/Vandenberghe_ASGPS-02.pdf.
- Wang, C., Y. Chen, M. Chen, and J. Shen, 2020: Data assimilation of a dense wind profiler network and its impact on convective forecasting. Atmos. Res., 238, 104880, https://doi.org/10.1016/j. atmosres.2020.104880.
- Wang, X., H. G. Chipilski, C. H. Bishop, E. Satterfield, N. Baker, and J. S. Whitaker, 2021: A multiscale local gain form ensemble transform Kalman filter (MLGETKF). *Mon. Wea. Rev.*, 149, 605–622, https://doi.org/10.1175/MWR-D-20-0290.1.
- Wang, Y., and X. Wang, 2017: Direct assimilation of radar reflectivity without tangent linear and adjoint of the nonlinear

- observation operator in the GSI-based EnVar system: Methodology and experiment with the 8 May 2003 Oklahoma City tornadic supercell. *Mon. Wea. Rev.*, **145**, 1447–1471, https://doi.org/10.1175/MWR-D-16-0231.1.
- Weckwerth, T. M., and D. B. Parsons, 2006: A review of convection initiation and motivation for IHOP_2002. Mon. Wea. Rev., 134, 5–22, https://doi.org/10.1175/MWR3067.1.
- —, and U. Romatschke, 2019: Where, when, and why did it rain during PECAN? Mon. Wea. Rev., 147, 3557–3573, https://doi.org/10.1175/MWR-D-18-0458.1.
- —, J. W. Wilson, and R. M. Wakimoto, 1996: Thermodynamic variability within the convective boundary layer due to horizontal convective rolls. *Mon. Wea. Rev.*, 124, 769–784, https://doi.org/10.1175/1520-0493(1996)124<0769:TVWTCB>2.0.CO;2.
- White, B. L., and K. R. Helfrich, 2012: A general description of a gravity current front propagating in a two-layer stratified fluid. J. Fluid Mech., 711, 545, https://doi.org/10.1017/jfm.2012.409.
- Wilson, J. W., and R. D. Roberts, 2006: Summary of convective storm initiation and evolution during IHOP: Observational and modeling perspective. *Mon. Wea. Rev.*, 134, 23–47, https://doi. org/10.1175/MWR3069.1.
- World Meteorological Organization, 2018: Statement of guidance for high-resolution numerical weather prediction (NWP). WMO Rep., WMO, 10 pp.
- Wulfmeyer, V., and Coauthors, 2015: A review of the remote sensing of lower tropospheric thermodynamic profiles and its indispensable role for the understanding and the simulation of water and energy cycles. *Rev. Geophys.*, 53, 819–895, https://doi.org/10.1002/2014RG000476.
- Yoshida, S., S. Yokota, H. Seko, T. Sakai, and T. Nagai, 2020: Observation system simulation experiments of water vapor profiles observed by Raman lidar using LETKF system. SOLA, 16, 43–50, https://doi.org/10.2151/sola.2020-008.
- Zhang, J., and Coauthors, 2016: Multi-Radar Multi-Sensor (MRMS) quantitative precipitation estimation: Initial operating capabilities. *Bull. Amer. Meteor. Soc.*, 97, 621–638, https:// doi.org/10.1175/BAMS-D-14-00174.1.
- Zhang, L., and Z. Pu, 2011: Four-dimensional assimilation of multitime wind profiles over a single station and numerical simulation of a mesoscale convective system observed during IHOP_2002. Mon. Wea. Rev., 139, 3369–3388, https://doi.org/10.1175/2011MWR3569.1.
- Zuidema, P., G. Torri, C. Muller, and A. Chandra, 2017: A survey of precipitation-induced atmospheric cold pools over oceans and their interactions with the larger-scale environment. *Surv. Geophys.*, 38, 1283–1305, https://doi.org/10.1007/s10712-017-9447-x.